Appl. Phys. B 77, 149–165 (2003)
DOI: 10.1007/s00340-003-1214-7

Applied Physics B
Lasers and Optics

V.P. KANDIDOV[1]
O.G. KOSAREVA[1,✉]
I.S. GOLUBTSOV[1]
W. LIU[2]
A. BECKER[3]
N. AKOZBEK[4]
C.M. BOWDEN[5]
S.L. CHIN[2]

Self-transformation of a powerful femtosecond laser pulse into a white-light laser pulse in bulk optical media (or supercontinuum generation)

[1] International Laser Center, Physics Department, Moscow State University, Moscow, 119992, Russia
[2] Departement de Physique, de Genie Physique et d'Optique and Centre d'Optique, Photonique et Laser, Universite Laval, Quebec G1K 7P4, Canada
[3] Max-Planck-Institut für Physik komplexer Systeme, Nöthnitzer Str. 38, 01187 Dresden, Germany
[4] Time Domain Corporation, 7057 Old Madison Pike, Huntsville, AL 35 806, USA
[5] US Army Aviation and Missile Command, AMSAM-WS-RD-ST, Huntsville, AL 35 898-5000, USA

Received: 24 February 2003/Revised version: 30 April 2003
Published online: 14 August 2003 •

ABSTRACT We present experimental and theoretical results on white-light generation in the filamentation of a high-power femtosecond laser pulse in water and atmospheric air. We have shown that the high spatio-temporal localization of the light field in the filament, which enables the supercontinuum generation, is sustained due to the dynamic transformation of the light field on the whole transverse scale of the beam, including its edges. We found that the sources of the supercontinuum blue wing are in the rings, surrounding the filament, as well as at the back of the pulse, where shock-wave formation enhanced by self-steepening takes place. We report on the first observation and demonstration of the interference of the supercontinuum spectral components arising in the course of multiple filamentation in a terawatt laser pulse. We demonstrate that the conversion efficiency of an initially narrow laser pulse spectrum into the supercontinuum depends on the length of the filament with high intensity gradients and can be increased by introducing an initial chirp.

PACS 42.65.Jx; 42.65.Re; 42.25.Bs; 42.50.Hz

1 Introduction

Propagation of a high-peak-power ultra-short laser pulse through bulk transparent media is accompanied by the strong modification of its spatial and temporal properties. Transformation of the pulse into the frequency domain, in particular the appearance of a large frequency sweep, which can extend from the ultraviolet to the infrared range (supercontinuum generation [1] or a white-light laser pulse [2]), is the spectral representation of the spatio-temporal modification of the radiation in the nonlinear medium.

Earlier experiments on the nonlinear pulse transformation and broadening of the frequency spectrum were performed with nano- and picosecond pulses focused in condensed media [3]. Advancement of laser technology creating femtosecond pulses with peak power up to many terawatts made possible the observation of the nonlinear pulse shape and spectral transformation in gaseous media. One of the first observations of spectral superbroadening from ~ 400 to ~ 800 nm in gases was performed in [4], where 70-fs and 2-ps dye laser pulses centered at 600 nm were focused in Xe and N_2 gases at 30-atm pressure.

Self-transformation of the pulse shape and spectral broadening are the result of strong nonlinear-optical interaction of the light field with the medium, which takes place in the conditions of high localization of the radiation both in space and time. There might be several ways to localize the light field inside the medium. One possible way is to take advantage of an optical device. With such devices as capillaries, microstructured fibers, and photonic crystals it is possible to govern the mode dispersion and to achieve high localization of the light field at comparatively long interaction distances (see e.g. [5–7]). Akimov et al. [8] reported the first observation of the spectral superbroadening (up to 400 nm) of an 800-nm, 40-fs pulse with subnanojoule energy in a tapered fiber. Thus, one of the important advantages of the supercontinuum generation in microstructured fibers and photonic crystals is the relatively low input pulse energy required for the registration of the phenomenon.

In bulk media the localization of the light field is achieved due to geometrical focusing, self-focusing, or temporal compression of the radiation. This localization may persist for long distances. In the first experiments on the propagation in air of pulses generated by Ti:sapphire laser amplification systems with peak powers of 5–50 GW, duration 100–250 fs, central wavelength 700–800 nm, and collimated input beam intensity distribution, the phenomenon of filamentation was observed. In the course of filamentation 9%–12% of the input pulse energy was localized in the filament – a narrow near-axis region with the transverse diameter of the order of 100 μm and a longitudinal scale of several tens of meters [9–11]. Later on, a more than two-hundred-meter filament was obtained in the propagation of a 60-fs pulse centered at 795 nm with a peak power of 300 GW [12]. With a terawatt peak power of the Ti:sapphire laser system and a 120-fs pulse duration the filaments and accompanying spectral broadening were registered not only in air but also in the atmospheric density rare gases [13]. There were observations of filamentation at the laser central wavelength different from 790–800 nm. In par-

✉ Fax: +7-095/939-3113, E-mail: kosareva2003@mail.ru

ticular, in [12] the experiment was also performed with 1-ps pulses at 1053 nm and in [14] 450-fs pulses at 248 nm were used. The analysis shows that the extended localization of energy, i.e. filamentation, is the result of dynamic competition between the Kerr self-focusing of the radiation and its nonlinear defocusing in the self-produced laser plasma [11, 15–17]. The length of the nonlinear interaction in the filament can be long enough to transform the essential part of the input pulse energy into a wide range of spectral frequencies. An important advantage of supercontinuum generation in bulk media is the possibility to obtain a wide spectrum inside the medium under investigation (e.g. in atmospheric air or oceanic water) and to deliver the resulting coherent white light, or a white-light laser pulse [2], to the prescribed position, which can be at a very large distance from the laser source.

The frequency spectrum produced in the course of a long-range filamentation of high-power femtosecond laser pulses in the atmosphere incorporates nearly all typical features of the supercontinuum, which will be discussed in more detail in Sect. 2. These features are a large blue wing produced mainly due to free-electron generation, a red wing created due to the combined effect of instantaneous and delayed responses of the Kerr nonlinearity, and an angular distribution of spectral wavelengths in the form of conical emission. A spectrum that extends from 300 nm to 4.5 μm after the propagation of both 35-fs, 60-mJ and 100-fs, 100-mJ laser pulses centered at 800 nm was obtained in [18] in atmospheric air. In the first femtosecond lidar experiments [19, 20], time-resolved broadband spectroscopy was performed on the supercontinuum backscattered from the atmosphere from the height of more than 1000 m. High-resolution spectra of the range-resolved atmospheric transmission showed the ro-vibrational H_2O and molecular oxygen absorption transitions. Thus, a coherent white light, accompanying filamentation in air, proved to be a novel light source for atmospheric remote sensing.

The purpose of this paper is to present our experimental and theoretical studies of the self-transformation of a femtosecond laser pulse into a white-light laser pulse in bulk condensed and gaseous media by the example of water and atmospheric air, respectively. We consider the joint effect of such physical mechanisms as Kerr nonlinearity, ionization, group-velocity dispersion as well as initial pulse parameters such as wavefront curvature and frequency chirp on the nonlinear spatio-temporal transformation and the corresponding frequency-angular spectrum of the pulse. By the frequency-angular spectrum of the pulse we mean spatio-temporal Fourier transform of the complex light field amplitude (see (15) in Sect. 4 of this paper).

2 Mechanisms for supercontinuum generation

Let us consider possible mechanisms for the formation of the new frequencies in the continuum spectrum of a self-transformed laser pulse. By the term 'supercontinuum generation' we understand the continuum range of all the new frequencies, which arise due to the nonlinear transformation of the pulse in the medium and we exclude the spectrum of the initial laser pulse. At the same time, the term 'white-light laser pulse' encompasses the whole spatio-temporal light-field distribution and, consequently, the modified frequency spectrum that was created after the propagation in the nonlinear medium. This total light-field distribution also includes the spectrum of the initial laser pulse.

One of the first explanations of ultra-short laser pulse spectrum transformation was done on the basis of a simple model, where the maximum relative broadening $\Delta\omega/\omega_0$ was directly proportional to the pulse intensity in the medium with instantaneous Kerr nonlinearity [21]. The frequency deviation $\delta\omega(\tau) = -kz\partial\Delta n/\partial\tau$ (here Δn is the nonlinear contribution to the refractive index, τ is the pulse duration, z is the propagation coordinate, and k is the wave number) is symmetric relative to the peak of the pulse. Therefore, the spectral broadening is also symmetric relative to the laser central frequency. In this model the radiation is considered to be a plane wave with a given temporal distribution. The spatial distribution of the radiation in the transverse direction was not taken into account. Later on, it was concluded that self-focusing played an essential role in spectral superbroadening [4, 22, 23]. Indeed, the simple self-phase-modulation model, which neglects the spatial effects, could not explain the increase of the spectral width $\Delta\omega$ up to several hundred nanometers, observed in the experiments.

Further experimental studies have shown that not only self-focusing but also geometrical focusing of the pulse into the medium influence the width of the frequency spectrum [24]. It was demonstrated that the threshold of the supercontinuum produced by a 1-ps, 593-nm pulse focused in 20-atm CO_2 gas increases with the decrease in the geometrical focal length of the lens. This threshold increase was associated with the defocusing of the radiation by the plasma, produced in the vicinity of the geometrical focus. The shorter the focal length of the lens, the stronger was the scattering of the radiation by the plasma. The same conclusion was obtained in recent experiments using 45-fs, 800-nm laser pulses on the competition between filamentation and multiphoton/tunnel ionization (in air [25]) and optical breakdown (in condensed matter, water [51, 61], and fused silica [26]).

At the same time, the free-electron generation contributes essentially to the spectral transformation. The frequency deviation $\delta\omega(\tau) = -kz\partial\Delta n/\partial\tau$ is positive due to the negative contribution to the refractive index Δn from the free electrons, the density of which grows during the pulse. The spectral broadening is asymmetric and blue shifted relatively to the laser central frequency [27–30]. Ionization and optical breakdown (the latter often follows the ionization in dense gases or condensed media) strongly depend on the pulse peak intensity.

In the conditions of tight focusing of the radiation into the medium, where the third-order nonlinear susceptibility is comparatively low (e.g. in the noble gases), the major contribution to the spectral transformation comes from the free electrons. Experimentally, this phenomenon was studied in [28, 29] and numerically in [29–31]. The extension of the blue wing formed after the tight focusing of a 100-fs pulse with the central wavelength of 620 nm into the noble gases varied from ≈ 15 nm in 1-atm argon, krypton, and xenon to ≈ 50 nm when these gases were at 5-atm pressure. Spectral blue shifting is accompanied by the spatial defocusing of the radiation and the formation of rings in the trailing part of the pulse [32]. It was found as the result of numerical simulations [31, 33] and registered experimentally [34,

35] that the blue-shifted components of the frequency spectrum are formed at the off-axis position in the transverse distribution of the radiation. A larger frequency shift is generated at positions farther from the propagation axis. Thus, the spectrum of the pulse is transformed not only in the frequency domain but also in the domain of the spatial wave numbers.

Spatial characteristics of the white light generated in condensed media, in particular in H_2O and D_2O, were studied in [36]. The supercontinuum was produced by focusing a 22-ps pulse at 1.06 μm of up to 35-mJ energy into water. Independently of the focal length of the lens used to focus the radiation into the cell, the supercontinuum was spread out in a circular rainbow with frequency increasing with the increase in the off-axis angle. Golub [36] interprets the observed phenomenon – the *supercontinuum cone emission* – as the radiation emitted from the surface of self-trapped filaments at angles that satisfy the Cerenkov relation.

Another possible explanation of the frequency angular distribution of the supercontinuum was suggested in [37], where the increase of the off-axis angle with increasing spectral frequency of a 100-fs, 1-μJ pulse focused into ethylene glycol was attributed to four-photon parametric generation on the surface of a small-scale filament. Numerical simulations of the pulse propagation in the conditions of self-focusing and normal group-velocity dispersion [38] also propose that the short-pulse supercontinuum conical emission is the result of four-wave mixing in the medium. However, according to these simulations, conical emission should also exist in the Stokes part of the spectrum. The latter fact was not observed in the experiments. According to [2, 39] the conical emission is the result of spatio-temporal self-phase modulation of a femtosecond pulse propagating in the conditions of self-focusing and plasma production. The temporal phase gradient $\partial\varphi/\partial\tau$, which defines the frequency deviation $\delta\omega(\tau)$, is, as was mentioned earlier, proportional to the time derivative of the electron density: $\delta\omega(\tau) = \partial\varphi/\partial\tau \sim \partial N_e(\tau)/\partial\tau$. At the same time, the spatial phase gradient, $\partial\varphi/\partial r$, which defines the transverse component of the wave vector δk_r, is proportional to the radial derivative of the electron density: $\delta k_r = \partial\varphi/\partial r \sim |\partial N_e(r)/\partial r|$. In the course of the nonlinear interaction high spatio-temporal gradients of free-electron density arise simultaneously in space and time. As a result, high-frequency spectral components propagate at a larger angle to the propagation direction.

We have discussed the possible origin and angular distribution of the supercontinuum blue wing. There could also exist an asymmetric extension to the Stokes side or a red shift of the pulse frequency spectrum. One of the reasons for the Stokes spectral broadening is the noninstantaneous Kerr response of the neutral medium. The physical mechanism of it is a nuclear response due to rotational and vibrational motions. The calculations and experiment performed in [40] showed that the response time of the rotational Raman molecular nonlinearity in molecular gases O_2 and N_2 is approximately 70 fs. The combination of an instantaneous electronic Kerr nonlinearity and a delayed rotational Raman molecular response leads to a steeper leading edge in the positive time-dependent change of the refractive index as compared with the trailing edge. As a result, the frequency deviation $\delta\omega(\tau) = -kz\partial\Delta n/\partial\tau$ is larger on the Stokes side and the spectrum exhibits a red-enhanced part.

In the conditions of a strong localization of energy that enables us to obtain an efficient redistribution of input laser pulse energy into the supercontinuum energy, there exists an additional mechanism that enhances the blue part of the pulse spectrum [41]. This mechanism is temporal self-steepening of the radiation and shock-wave formation at the trailing edge of the pulse. As a result, the positive frequency deviation $\delta\omega(\tau) = -kz\partial\Delta n/\partial\tau$ at the back of the pulse is larger than the absolute value of the negative frequency deviation at the front of the pulse. The spectrum acquires a large blue pedestal due to a purely positive nonlinear contribution to the refractive index from the Kerr nonlinearity [42–45]. The effect is the stronger the shorter is the input pulse duration. Self-steepening of the pulse can explain the formation of the blue spectral wing in the propagation of ultra-short pulses through microstructured fibers [46]. In these optical devices a steep trailing edge of the subpulse formed inside the fiber may originate due to the joint influence of higher-order dispersion terms (≥ 3) and the Kerr nonlinearity.

In summary, the effect of various physical mechanisms on spectral broadening can be interpreted in terms of spatio-temporal self-phase modulation. Indeed, for the instantaneous electronic Kerr response, the 'nonlinear' phase is directly proportional to the intensity. In the case of free-electron generation, the electron density, growing as a function of the intensity, influences the 'nonlinear' phase through the plasma contribution to the refractive index. Stimulated Raman scattering on rotational transitions in molecular gases results in the delayed response of the Kerr nonlinearity and also leads to the intensity-dependent phase of the pulse. Self-steepening increases the 'nonlinear' phase gradients through the increase of intensity gradients on the pulse fronts. Such mechanisms as self-focusing and ionization affect not only longitudinal but also the transverse electric field distribution and, therefore, the transverse spatial phase of the pulse. This gives rise to such phenomena as the supercontinuum conical emission.

3 Experimental setups for ultra-short high-power pulse generation

In the experiments we used a Ti:sapphire laser system (Fig. 1a) that emits three simultaneous beams. The system consists of an oscillator (Maitai, 28 fs at 80 MHz, Spectra Physics), followed by a stretcher and a regenerative amplifier (Spitfire, Spectra Physics), which works at 1-kHz repetition rate. A two-pass amplifier enhances the output from the regenerative amplifier. The amplified beam is compressed to 40 fs and gives a maximum energy of 2 mJ/pulse at 1 kHz. On the other hand, just after the regenerative amplifier, a pulse slicer is used to pick up one pulse every 100 ms. This 10-Hz seed beam is again split into two beams by a beam splitter. One part of the seed beam is sent to a two-pass amplifier and compressed by a portable compressor. After the portable compressor, 10-Hz laser pulses with an energy of 20 mJ/pulse and 42-fs duration are obtained. The second 10-Hz seed beam is sent to a four-pass amplifier, which is followed by a vacuum compressor. Through a 10-m-long pipe with a 1-cm-thick CaF_2 window at the end, our vacuum compressor is connected

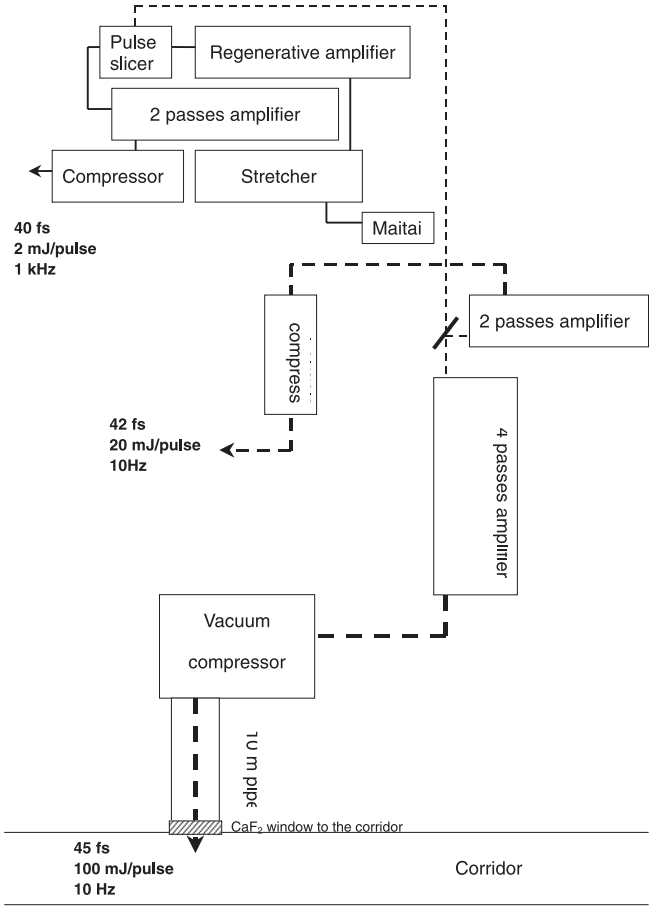

FIGURE 1 **a** Ti:sapphire laser system that emits three beams simultaneously: 40 fs, 2 mJ per pulse at 1-kHz repetition rate, 42 fs, 20 mJ per pulse at 10-Hz repetition rate, 45 fs, 100 mJ per pulse at 10-Hz repetition rate. **b** Experimental setup used for supercontinuum generation in water

to the 200-m-long corridor. At the exit of the pipe, we can have a 45-fs laser pulse and up to 100-mJ pulse energy. The typical spectrum of all three beams is centered at 810 nm with a spectral width of 32 nm (FWHM).

For the experiments on the supercontinuum generation in water a 1-kHz beam with a maximum energy of 2 mJ per pulse was used (Fig. 1b). The input pulse energy was controlled by a half-wave plate, which was located before the compressor. The laser pulse was focused by a microscope objective into a glass water cell. The transmitted pulse spectrum is collimated after the cell by an achromatic lens and imaged onto the slit of the spectrometer. Frequency spectra obtained after the propagation in water are discussed in Sect. 6.

4 Theoretical model for the nonlinear-optical pulse transformation

Transformation of the shape and the spectrum of a femtosecond laser pulse results from the nonlinear-optical interaction of the light field with the medium, which is defined by a number of factors: Kerr self-focusing, ionization of the medium, material dispersion, diffraction, and self-steepening.

Theoretical models, which describe the effect of all the factors on the laser pulse propagating in transparent dielectrics, are based on the scalar approximation of the wave equation for the light field $q(x, y, z, t)$ in the dispersive medium [47]:

$$\left(\frac{\partial^2}{\partial z^2}+\Delta_\perp\right)q-\frac{1}{c^2}\frac{\partial^2}{\partial t^2}\int\limits_{-\infty}^{t}\partial t'\varepsilon(t-t')q(t') = \frac{4\pi}{c^2}\left(\frac{\partial j}{\partial t}+\frac{\partial^2 p_{\mathrm{nl}}}{\partial t^2}\right), \quad (1)$$

where p_{nl} is the nonlinear polarization of the neutral atoms and molecules in the medium and j is the current of the free charges produced due to the ionization in the high-intensity laser field.

In order to obtain the first-order equation relative to the propagation coordinate z, let us represent the light field $q(x, y, z, t)$ in the form of the wave packet with the carrier frequency ω_0:

$$q(x, y, z, t) = E(x, y, z, t)\exp i(\omega_0 t - kz), \quad (2)$$

where $E(x, y, z, t)$ is the slowly varying complex amplitude of the light field. Complex amplitudes of the nonlinear polarization P_{nl} and the field current J at the frequency ω_0 are given by the equations:

$$P_{\mathrm{nl}} = \frac{n_0}{\pi}\Delta n_k(I)E, \quad (3)$$

$$\frac{\partial J}{\partial t} = \frac{\mathrm{e}^2}{m_{\mathrm{e}}}N_{\mathrm{e}}(I)E+\frac{cn_0}{4\pi}\frac{\partial}{\partial t}(\alpha(I)E), \quad (4)$$

where n_0 is the unperturbed refractive index of the medium, $\Delta n_{\mathrm{k}}(I)$ is the contribution of the electronic and nuclear response of the Kerr nonlinearity, $N_{\mathrm{e}}(I)$ is the free-electron density, the change of which in space and time is defined by the rate equations for the photo-ionization, $I = cn_0|E|^2/8\pi$, and m_{e} and e are the electron mass and charge, respectively. The absorption coefficient $\alpha(I)$ that describes the ionization energy loss is:

$$\alpha = I^{-1}m\hbar\omega_0\left(\frac{\partial N_{\mathrm{e}}(r, z, t)}{\partial t}\right), \quad (5)$$

where m is the order of the multiphoton process.

Following [42], we can obtain from (1)–(4) the nonlinear equation for the complex amplitude $E(x, y, z, t)$, which in the retarded coordinate system ($\tau = t - z/v_g$) takes the

form [44, 45]:

$$2ik\frac{\partial E}{\partial z} = \left(1 - \frac{i}{\omega_0}\frac{\partial}{\partial \tau}\right)^{-1} \Delta_\perp E - kk''_\omega \frac{\partial^2 E}{\partial \tau^2} + \frac{i}{3}kk'''_\omega \frac{\partial^3 E}{\partial \tau^3} + \frac{2k^2}{n_0}\left[\left(1 - \frac{i}{\omega_0}\frac{\partial}{\partial \tau}\right)\Delta n_{\rm k} + \left(1 + \frac{i}{\omega_0}\frac{\partial}{\partial \tau}\right)\Delta n_p\right] E - ik\alpha E\,. \tag{6}$$

The first term on the right-hand side of (6) describes the beam diffraction; the second and the third terms describe material dispersion. Note that in the conditions of strong self-focusing and self-steepening, material dispersion should be considered up to the third order or higher, because the higher-order dispersion terms influence the formation of subpulses [45]. The fourth term describes the contribution of the Kerr nonlinearity and the plasma to pulse transformation. The fifth term describes the pulse energy loss due to the ionization.

Equation (6) for the complex amplitude of the electric field E, unlike the wave equation in the slowly varying envelope approximation (SVEA) [41], contains the operator $[1 \pm (i/\omega_0)(\partial/\partial\tau)]$, which appears after the substitution of (2)–(4) into (1) and retaining the higher-order terms in comparison with the SVEA. This approximation with the higher-order correction terms is called *the slowly evolving wave approximation* (SEWA) [42]. It was shown in [42] that in the framework of the SEWA the equation for the complex amplitude of the electric field E accurately describes light-pulse propagation down to the single-cycle regime. For this pulse the spectral width is comparable to the carrier frequency ω_0. When applied to the problem of nonlinear-optical transformation of an ultra-short high-power pulse, the SEWA adequately reproduces the formation of a wide broadened spectrum of the radiation. In terms of mechanisms that contribute to the modification of ultra-short radiation, the SEWA describes self-steepening of the pulses and subpulses arising in the course of propagation as well as the shock-wave formation at the back of the pulse.

The Kerr nonlinearity of neutrals far from the atomic and molecular resonances is defined by an anharmonic response of the bound electrons and the stimulated Raman scattering on rotational transitions of molecules. In the case of femtosecond pulses, the electronic response may be considered as instantaneous. The contribution from the stimulated Raman scattering is nonstationary, as shown theoretically in [48] and experimentally and theoretically in [40]. In [16], the response function $H(t)$ measured in [40] was approximated based on the damped oscillator model by the following equation:

$$H(t) = \theta(t)\Omega^2 \exp(-\Gamma t/2)\sin(\Lambda t)/\Lambda\,, \tag{7}$$

where $\theta(t)$ is the Heaviside function and $\Lambda = \sqrt{\Omega^2 - \Lambda^2/4}$. The fitting parameters have the following values: $\Omega = 20.6$ THz and $\Gamma = 26$ THz. The corresponding characteristic times $\tau_1 = 2/\Gamma$ and $\tau_2 = 1/\Lambda$ are $\tau_1 = 77$ fs and $\tau_2 = 62.5$ fs. These values are comparable with the laser-pulse duration used in the recent laboratory experiments on the observation of filamentation and supercontinuum generation [9–14, 18–20].

Finally, the nonlinear contribution to the refractive index from the neutral molecules is considered in the form:

$$\Delta n_{\rm k}(t) = (1-g)\frac{1}{2}n_2 |E|^2 + g\int\limits_{-\infty}^{t} \frac{1}{2}n_2 \left|E(r,t')\right|^2 H(t-t')\,{\rm d}t'. \tag{8}$$

The nonlinear contribution to the refractive index $\Delta n_{\rm p}(x, y, z, t)$ from the laser-produced plasma is given by:

$$\Delta n_{\rm p}(x,y,z,t) = -\frac{\omega_{\rm p}^2(x,y,z,t)}{2n_0(\omega_0^2+\nu_c^2)}\left(1 - i\frac{\nu_c}{\omega_0}\right), \tag{9}$$

where $\omega_{\rm p}(x, y, z, t) = \sqrt{4\pi\, {\rm e}^2 N_{\rm e}(x, y, z, t)/m_{\rm e}}$ is the plasma frequency, $\nu_c = N_0 v_{\rm e}\sigma_c$ is the effective electron collision frequency with the root-mean-square electron velocity $v_{\rm e}$ and the electron collision cross section σ_c, and N_0 is the density of neutrals.

The free-electron density $N_{\rm e}(x, y, z, t)$ depends on the spatial coordinates and time according to the kinetic equation:

$$\frac{\partial N_{\rm e}}{\partial t} = R(|E|^2)(N_0 - N_{\rm e}) + \nu_i N_{\rm e} - \beta N_{\rm e}^2, \tag{10}$$

where N_0 and $R\left(|E|^2\right)$ are the density and the ionization rate of neutrals, respectively and β is the radiative electron-recombination coefficient. The avalanche ionization frequency is:

$$\nu_i = \frac{1}{W}\frac{{\rm e}^2 E^2}{2m_{\rm e}(\omega_0^2+\nu_c^2)}\nu_c, \tag{11}$$

where W is the ionization potential in the case of a gaseous medium or the band gap in the case of condensed media.

Equation (10) is written in the single-ionization approximation. This approximation can be applied to the study of ultra-short pulse propagation in air since the ionization degree $N_{\rm e}/N_0$ is less than 0.001 [49, 50]. In water the ionization degree reaches 0.02 due to the essential contribution of the avalanche ionization even in the case of an ultra-short 45-fs pulse [51].

In the case of a femtosecond pulse propagation in atmospheric density gases, the effective electron–neutral collision frequency ν_c is much smaller than the laser frequency ω_0 [52], and (9) for the plasma contribution to the refractive index takes the form:

$$\Delta n_{\rm p}(x,y,z,t) = -\frac{\omega_{\rm p}^2(x,y,z,t)}{2n_0\omega_0^2}. \tag{12}$$

In the atmospheric air the large amount of free electrons comes from the oxygen molecules, the ionization potential of which $W_{\rm O_2} = 12.1$ eV is smaller than the ionization potential of the nitrogen molecules $W_{\rm N_2} = 15.6$ eV [53]. To calculate the ionization rate $R\left(|E|^2\right)$ in (10) we used the model [54] for the ionization of a hydrogen-like atom in a linearly polarized electric field E:

$$R = |C_{n^*l^*}|^2\, f_{lm} E_j \sqrt{\frac{6}{\pi}}\left(\frac{2\,(2W)^{3/2}}{E}\right)^{2n^*-|m|-3/2} \times \left(1+\gamma^2\right)^{|m|/2+3/4} A_m(\omega_0,\gamma)\,{\rm e}^{-\frac{2(2W)^{3/2}}{3E}g(\gamma)}. \tag{13}$$

Here $\gamma = \omega_0\sqrt{2W}/E$ is the Keldysh parameter, $n^* = Z/\sqrt{2E_i}$ is the effective main quantum number, $l^* \approx n^* - 1$ is the effective orbital quantum number, Z is the effective ion charge, l is the orbital quantum number, and m is the projection of the orbital quantum number on the direction of the electric field vector. The coefficients $C_{n^*l^*}$ and f_{lm} as well as the functions $A_m(\omega_0, \gamma)$ and $g(\gamma)$ can be found in [55]. The values of effective charges for the ionization of oxygen and nitrogen molecules are calculated in [55] by fitting (13) to the experimental data on molecular ion yields. They are equal 0.53 and 0.9 for oxygen and nitrogen molecules, respectively.

The pulse shape and beam profile at the femtosecond laser system output are close to Gaussian; therefore, the initial distribution of the electric field complex amplitude in the retarded coordinate system is described by:

$$E(x, y, z = 0, \tau) = E_0\sqrt{\frac{\tau_0}{\tau_\mathrm{p}(\delta)}} \times \exp\left(-\frac{x^2+y^2}{2a_0^2} - \frac{\tau^2}{2\tau_\mathrm{p}^2(\delta)} + i\frac{kr^2}{2R_f} + i\frac{\delta\tau^2}{2}\right), \quad (14)$$

where a_0 is the input beam pulse radius at $1/\mathrm{e}$ intensity level, R_f is the geometrical focusing distance, and τ_0 is a half-pulse duration of a transform-limited pulse at $1/\mathrm{e}$ intensity level. The parameter τ_0 is related to the full width at half maximum pulse duration τ_FWHM, which is usually measured in the experiments, as $\tau_0 = \tau_\mathrm{FWHM}/(2\sqrt{\ln 2})$. If at the output of the compressor the pulse is chirped, then the initial pulse duration $\tau_\mathrm{p}(\delta)$ depends on the parameter $\delta(\tau_\mathrm{p}(\delta = 0) = \tau_0)$, which characterizes the initial phase modulation of the pulse with a constant spectral width [41, 56].

The solution to the self-consistent problem (7)–(10), (13) with the initial conditions (14) defines the complex amplitude of the electric field $E(x, y, z, \tau)$ after the self-transformation of the pulse in the nonlinear dispersive medium. The frequency angular spectrum $S(\theta_x, \theta_y, \Delta\omega, z)$ at a distance z is calculated through the spatio-temporal Fourier transform as:

$$S(\theta_x, \theta_y, \Delta\omega, z) = \left|U(\theta_x, \theta_y, \Delta\omega, z)\right|^2,$$
$$U(\theta_x, \theta_y, \Delta\omega, z) = \int \mathrm{d}x\,\mathrm{d}y\,\mathrm{e}^{-i\theta_x kx}\,\mathrm{e}^{-i\theta_y ky} \times \int \mathrm{d}\tau\,\mathrm{e}^{-i\Delta\omega\tau}E(x, y, z, \tau), \quad (15)$$

where $\theta_x = k_x/k$, $\theta_y = k_y/k$ are the angles at which different frequency components $\Delta\omega$ propagate in the medium. In the visible part of the frequency spectrum and for the radially symmetric pulse distribution, the dependence of the angle $\theta = \theta_x = \theta_y$ on wavelength defines the supercontinuum cone emission. In order to represent the conical emission in the coordinates $\theta(\lambda)$, the following transition from spectral frequency to spectral wavelength is made: $\lambda = 2\pi c/(\omega_0 + \Delta\omega)$, where ω_0 is the laser central frequency. For the spatio-temporal frequency deviation as the function of time and radial coordinate, the corresponding spectral wavelengths are calculated according to the expression:

$$\lambda = 2\pi c/(\omega_0 + \partial\varphi/\partial\tau), \quad (16)$$

where φ is the phase of the complex amplitude of the electric field $E(r, \tau)$.

5 Supercontinuum generation in air

Supercontinuum generation in air is closely connected to the phenomenon of high-power femtosecond laser pulse filamentation. This phenomenon is characterized by the stabilization of the radiation parameters, which are available for measurements. Among such parameters are the filament diameter and energy. Both values are defined from the narrow near-axis part of the fluence distribution. In addition, the peak intensity and the maximum plasma density in the filament preserve the same values of $\sim 4 \times 10^{13}$ W/cm^2 [53, 57] and 10^{16} cm^{-3} [50], respectively. The clamping of the peak intensity inside the filament to a maximum value can be readily understood [53] to be due to a balance between the Kerr self-focusing and the plasma defocusing effects. It has been shown in gases by observing the plateau in high-harmonic generation for Xe [58] and by observing fluorescence spectra emitted from excited nitrogen molecules and molecular ions [57].

Fluence is an integrated characteristic of the propagation and its distribution does not reveal the mechanism of supercontinuum generation. In spite of the fact that the fluence is stabilized, a spatio-temporal intensity distribution in the filament is strongly nonstationary and experiences significant changes along the propagation. The narrow near-axis part (100 μm) of the pulse is fed from the wide (of the order of or larger than the input beam diameter) background of the radiation, which contains around 90% of the total pulse energy. The dynamic process of the energy replenishment in the filament in the conditions of the Kerr nonlinearity, the laser-produced plasma, natural beam divergence, material dispersion, and self-steepening leads to dramatic transformation of the intensity and phase of the light field on the whole transverse beam section, which exceeds the input beam diameter. This results in the superbroadening of the frequency spectrum and conical emission generation. In order to adequately model the self-transformation of the pulse shape and spectrum as well as to obtain quantitative agreement with the experimental data on the amount of energy in the filament, the peak electron density, the width of the frequency spectrum, and the conical emission angles, both the small-scale changes in the filament center and the large-scale changes in the background should be taken into account in the simulations.

The experiment on the study of supercontinuum cone emission was performed using a Ti:sapphire chirped pulse amplification laser system generating 250-fs (FWHM) laser pulses with the central wavelength of 800 nm (the geometry of the setup was similar to that shown in Fig. 1a except that the smaller bandwidth from the oscillator and the stretcher as well as gain narrowing allowed us to generate only the pulses longer than 100 fs FWHM). The beam radius at the output of the grating compressors was $a_0 = 3.5$ mm ($1/\mathrm{e}$ intensity level). The collimated beam was sent into the long hallway by means of several transport mirrors and propagated freely to the end of the hallway for a total distance of 111 m. In order to study the spatial structure of the white light accompanying filamentation, the cone angle of the various colors in the conical emission was measured. In the experimental setup we used

a 4-mm-diameter aperture that was centered on the beam axis and a razor blade that blocked off the filament. The conical emission was measured on a white screen placed at 20 m after the aperture. An interference filter with 10-nm bandwidth was placed after the razor blade. The radii of the colored half-rings were measured on the screen at the following wavelengths: 500, 550, 600, 650, 700, and 750 nm. No ring was observed at $\lambda > 800$ nm. The half-angle θ_λ of the conical emission was defined as the ratio of the radius r of the ring to the distance D from the aperture. Experimental results of the conical emission angles as a function of wavelength are shown in Fig. 2. The pulse energy for this measurement was 10 mJ.

To simulate the propagation we used the system of equations (7)–(8), (10), and (12) with an input spatio-temporal distribution of the electric field in the form of (14), where $\tau_0 = 150$ fs corresponds to 250 fs FWHM, intensity $I_0 = 10^{11}$ W/cm^2, beam radius $a_0 = 3.5$ mm, diffraction length $z_d = ka_0^2 = 96$ m, and $\delta = 0$. The pulse energy was 10 mJ and the peak power $P_{peak} = 38\,\mathrm{GW} = 6.3P_{cr}$, where P_{cr} is the critical power for self-focusing in air. The calculations were performed on a grid with nonequidistant steps in the radial direction [59]. The number of grid steps was 2048 in the time domain, 7000 along the propagation coordinate z, and 512 in the radial direction.

Redistribution of the intensity in the transverse spatial direction and in time is shown in Fig. 3, where the scale in the plane (r, τ) is chosen so that the equal-intensity contours at the beginning of propagation ($z = 0$) are concentric rings (Fig. 3a). At the start of the filament ($z = 0.29z_d \approx 28$ m) the peak intensity of the pulse is attained in the temporal slice with $\tau \geq 0$ due to the delayed response of the Kerr nonlinearity (8) (Fig. 3b). The value of the peak intensity reaches $\approx 4 \times 10^{13}$ W/cm^2 and the ionization starts to defocus the trailing part of the pulse. At $z = 0.32z_d \approx 31$ m (Fig. 3c) the intensity maximum shifts towards the leading part of the pulse; its value reaches 6×10^{13} W/cm^2. At the trailing part of the pulse rings are formed. By $z = 0.4z_d \approx 39$ m (Fig. 3d) the diameter of the outer ring exceeds the input beam diameter by a factor of two. At the leading part we can see the very intense slices between $\tau \approx -80$ fs and $\tau \approx -50$ fs located in the narrow near-axis part within the transverse diameter of less than 300 μm. These slices form the 'filament' itself, i.e. the structure that appears to a human eye as a string of light foci. Formation of a dynamic multipeak structure in the spatio-temporal domain of the pulse is revealed as the spectral broadening in the frequency angular domain.

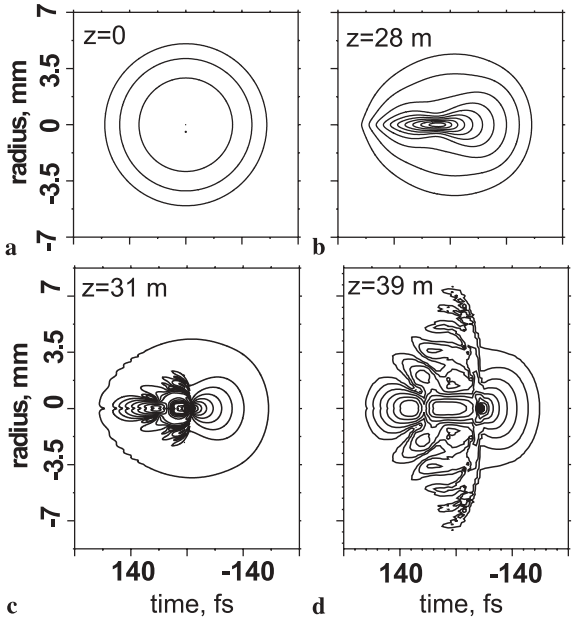

FIGURE 3 Spatio-temporal distribution of the laser pulse intensity $I(r, \tau)$ at different distances z from the laser system output. The equal-intensity contours are plotted for the following intensity values: $I_n = I_0 2^n$, where $n = -3, -2, \ldots, +9$, $I_0 \approx 10^{11}$ W/cm^2. **a** $z = 0$; **b** $z = 0.29z_d \approx 28$ m; **c** $z = 0.32z_d \approx 31$ m; **d** $z = 0.4z_d \approx 39$ m

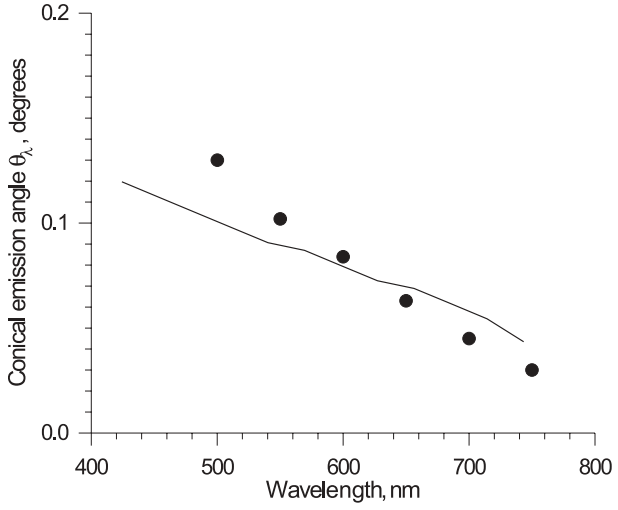

FIGURE 2 Dependence of the conical emission angle on wavelength in the blue wing of the pulse frequency spectrum. Experimental data [38] are shown by the *black dots* and the simulation results by the *solid curve*. Both in the experiment and in the simulations the pulse duration $\tau_0 = 150$ fs (250 fs FWHM), the pulse energy is 10 mJ (the ratio of the pulse peak power to the critical power for self-focusing $P_{peak}/P_{cr} = 6.3$), the input beam radius $a_0 = 3.5$ mm, and the propagation distance $z = 40$ m

Because of the correct consideration of the low-intensity background of the radiation, we were able to perform a quantitative comparison between the conical emission angles obtained in the experiment (Fig. 2, symbols) and in the simulations (Fig. 2, solid curve). Note that in the previous theoretical studies [2, 39] only the relative angles θ_λ/θ_0, where θ_0 is the input beam divergence, could be related to the experimental data. The quantitative discrepancy between the simulated and experimentally observed conical emission angles, which reaches $\approx 20\%$ for 500-nm wavelength, is due to the fact that for the numerical study in these particular experimental conditions we were not able to include material dispersion in the simulations. At the same time it has been shown by Golubtsov et al. [39] that the inclusion of the material dispersion leads to the increase of the conical emission angles.

For the understanding of the spectral superbroadening mechanism we study the sources of the supercontinuum in the pulse. In Fig. 4 we present the map of spectral wavelengths corresponding to the frequency deviation $\delta\omega(r, \tau) = \partial\varphi(r, \tau)/\partial\tau$ (see (16)). The distribution of wavelengths is presented together with the spatio-temporal intensity distribution $I(r, \tau)$ (equal-intensity contours are shown by solid lines). The upper inset in Fig. 4 shows the distribution of the elec-

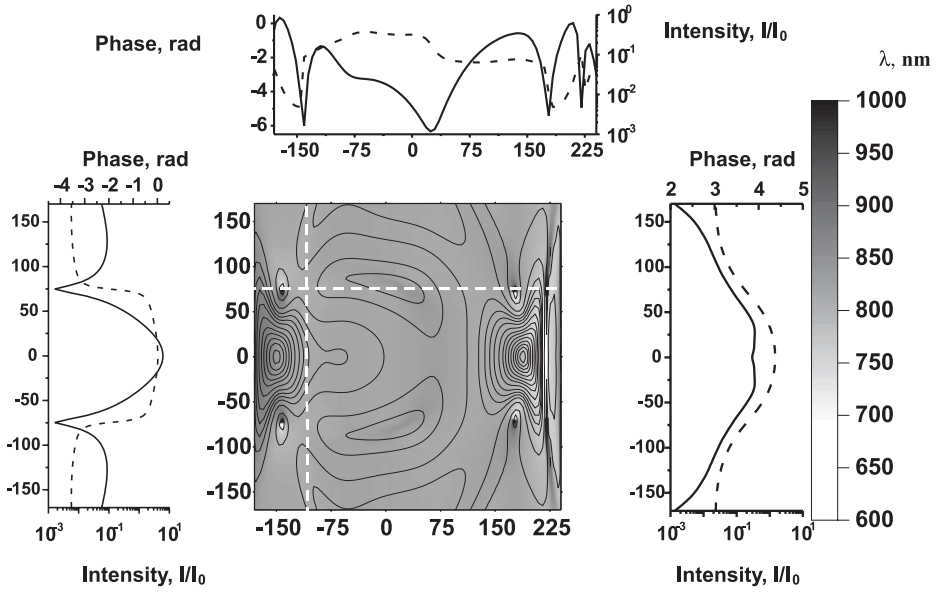

FIGURE 4 Spatio-temporal distribution of the supercontinuum sources. The *solid lines* correspond to the equal-intensity contours plotted for the following intensity values: $I_n = I_0 2^n$, where $n = -3, -2, \ldots, +9$, $I_0 \approx 10^{13}$ W/cm^2. The *upper inset* corresponds to the temporal distribution of the pulse intensity (*solid line*) and phase (*dashed line*) at $r = 73$ μm; the *left* and the *right insets* correspond to the radial distribution of the intensity (*solid line*) and the phase (*dashed line*) at $\tau = -140$ fs and $\tau = 217$ fs, respectively. Propagation distance $z = 0.76 z_d = 73$ m. Pulse parameters are the same as in Fig. 3. Radial position $r = 73$ μm and temporal positions $\tau = -140$ fs and $\tau = 217$ fs are indicated by the *white dashed lines* on the map

tric field intensity (solid line) and the phase (dashed line) as a function of time for the radial position $r = 73$ μm indicated by the white dashed horizontal line on the map. The left and the right insets in Fig. 4 show the distribution of the electric field intensity (solid line) and the phase (dashed line) as the function of the radial position at the leading ($\tau = -140$ fs) and the trailing ($\tau = 217$ fs) edges of the pulse. The temporal positions are indicated by the white dashed vertical lines on the map.

In Fig. 4 only the narrow near-axis part of the pulse distribution with the diameter of the order of 300 μm is presented. At this propagation distance $z = 0.76 z_d \approx 73$ m the intensity distribution reveals two peaks. The peak that is formed in the leading edge of the pulse $\tau = -140$ fs is due to the self-focusing in air and the peak at the trailing part $\tau = 180$ fs is formed due to the joint contribution of the refocusing and the delayed Kerr response. Two distinct ring sources of the short-wavelength components in the frequency spectrum can be seen on the map. Each ring source is represented by two white points located symmetrically relatively to the beam axis $r = 0$. The first is at the leading edge of the pulse, $\tau = -140$ fs, and its radius is 73 μm. This is the region where the Kerr-induced convergence is replaced by the plasma-induced divergence of the high-intensity slices. The time dependence of the phase along the white dashed line $r = 73$ μm shows the strong jump slightly before $\tau = -150$ fs and, hence, the positive frequency deviation $\delta\omega > 0$ (upper inset in Fig. 4). Note that, at the same moment $\tau = -150$ fs, the radial phase distribution reveals a large gradient $\partial\varphi/\partial r$ at the ring $r = 73$ μm (left inset in Fig. 4), which means that the new high frequencies born on this ring diverge at large angles to the propagation axis. Actually, this is how the conical emission originates from the nonlinear transformation of the pulse in the conditions of self-focusing and the plasma defocusing. The second supercontinuum source starts from the ring at the trailing edge of the pulse $\tau = 180$ fs, $r = 68$ μm and persists over the whole back front $\tau > 180$ fs. Here the positive frequency deviation $\delta\omega > 0$ is due to the shock formation at the back of the pulse, which can also be seen in the upper inset of Fig. 4, where the phase derivative $\partial\varphi/\partial\tau$ is positive at $\tau \geq 187$ fs. In the radial phase distribution at the back of the pulse ($\tau = 217$ fs, see the right inset in Fig. 4) the absolute value of the phase gradient $\partial\varphi/\partial r$ is much smaller than in the front of the pulse. In addition, there are no intensity rings corresponding to the radial phase jumps (compare the radial intensity distributions shown by the dashed lines in the left and the right insets in Fig. 4). Hence, the spatial distribution of the high-frequency components born due to self-steepening at the trailing edge of the pulse is not in the form of conical rings.

Figure 5 clearly demonstrates the role of self-steepening in the supercontinuum generation. In Fig. 5 the on-axis frequency spectrum for the case without self-steepening, i.e. without the operator $[1 \pm (i/\omega_0)(\partial/\partial\tau)]$ in (7), is plotted by the solid line and the spectrum obtained with the inclusion of this operator is plotted by the dotted line. For the on-axis spectrum

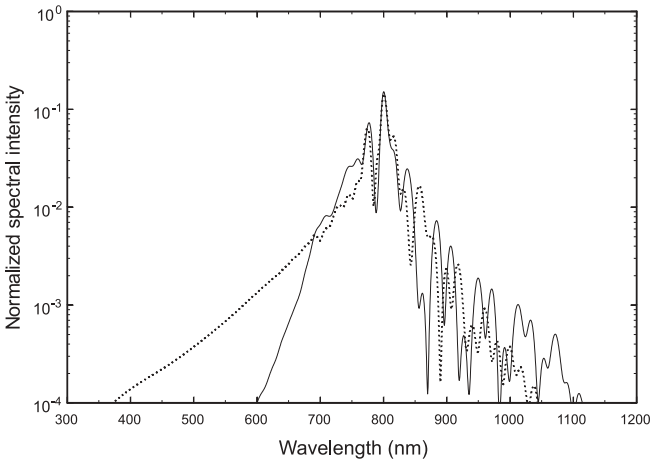

FIGURE 5 Frequency spectrum calculated on the beam axis without consideration of the self-steepening term $\pm(i/\omega_0)(\partial/\partial\tau)$ in (6) (*solid line*) and with the inclusion of this term so that $(\omega_0\tau_0)^{-1} = 0.007$ (*dotted line*). In the simulations the pulse duration was $\tau_0 = 90$ fs (150 fs FWHM), the ratio of the peak power to the critical power for self-focusing $P_{peak}/P_{cr} = 6$, the input beam radius $a_0 = 0.18$ mm, and $z = z_d$. The intensity is normalized to the peak input spectral intensity

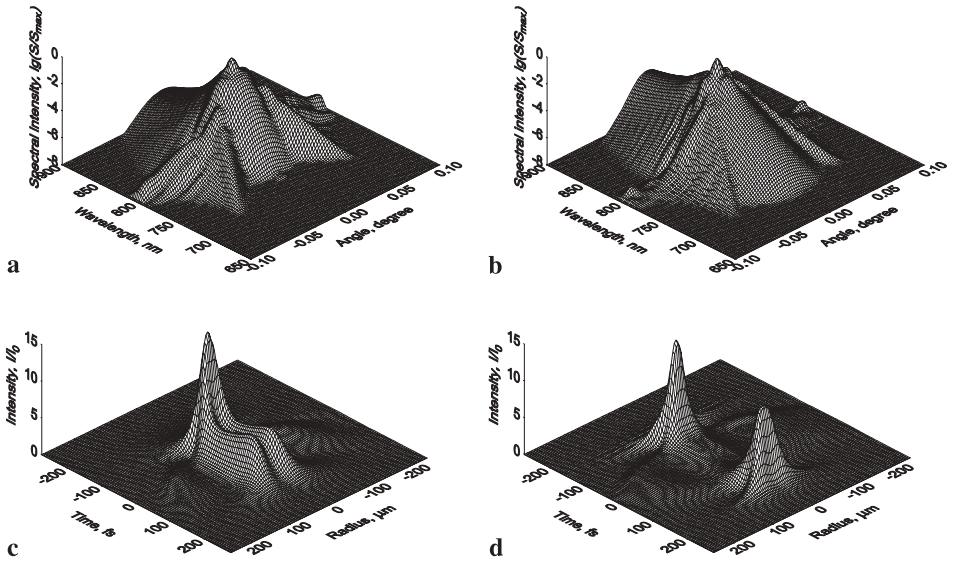

FIGURE 6 Frequency angular spectrum (**a**, **b**) and spatio-temporal distribution (**c**, **d**) of the pulse at two propagation distances: **a**, **c** $z = 0.43z_d$; **b**, **d** $z = 0.6z_d$. In the simulations the pulse duration was $\tau_0 = 150$ fs (250 fs FWHM), the ratio of the peak power to the critical power for self-focusing $P_{peak}/P_{cr} = 6.3$, and the input beam radius $a_0 = 0.18$ mm

at this propagation distance the effect of self-steepening leads to the increase of the blue wing by 250 nm at 10^{-4} level of the maximum intensity.

If the frequency spectrum is integrated over the whole transverse aperture, the relative contribution of self-steepening to the spectral broadening decreases [45]. The less pronounced effect of self-steepening in the case of the integrated spectrum is associated with the contribution of the high-frequency spectral components, which are generated at the off-axis positions mainly due to the laser-induced plasma production. This is confirmed by the frequency angular spectrum shown in Fig. 6a and b for the two distances $z = 0.43z_d$ and $z = 0.6z_d$ along the filament. The corresponding spatio-temporal intensity distribution are shown in Fig. 6 (c,d), respectively. The same figure demonstrates spatio-temporal intensity distributions at the corresponding propagation distances. At the beginning of the filamentation the blue wing is mainly formed in the ring at the leading edge of the pulse (compare with Fig. 4). Therefore, the conical divergence of high-frequency components dominates in the pulse spectrum (Fig. 6a). Later on, the pulse breaks up into the two subpulses. At the trailing edge of the second subpulse ($\tau = 140$ fs) the self-steepening is pronounced on the beam axis (Fig. 6d). As a result, the high-frequency components that appear in the pulse spectrum do not have the angular divergence and propagate mainly along the axis (Fig. 6b).

Thus, the supercontinuum generation in air strongly depends on the spatio-temporal phase gradients of the complex amplitude of the electric field. In Sect. 8 we will show how the phenomenon of long-range filamentation in air can allow us to control this spatio-temporal gradient and provide the most effective redistribution of energy to the supercontinuum energy in the prescribed position in the propagation.

6 Supercontinuum generation in water

Supercontinuum generation in water occurs already at low (megawatt) peak input powers, since the nonlinear refractive index is larger than that of air. The first set of experiments in water was performed with the pulses generated by the laser system similar to the one shown in Fig. 1a but with narrower bandwidth components that allowed us to generate only the pulses longer than 100 fs FWHM. The pulse duration was 170 fs FWHM and the energy varied from 0.2 to 200 μJ. The beam diameter at $1/e^2$ level was 4 mm. According to the scheme in Fig. 1b, the beam was focused with a 119-cm lens into a cell filled with water. Further details of the experimental setup can be found in [60]. Spectra obtained at low and high input laser energies are shown in panels (a) and (b) of Fig. 7 respectively. Each spectrum is normalized to its maximum at the central wavelength of 800 nm. While the spectra at low energies show a symmetrical broadening towards lower and higher frequencies, we observe the typical long pedestal on the blue side at higher pulse energies (note that the bandwidth of the spectrometer limited the observations on the red side to wavelengths below 1015 nm). The minimum wavelength of the blue spectral wing remains almost constant for an increase in the pulse energy by two orders of magnitude from 0.4 to 200 μJ (this wavelength is well within the bandwidth of the blue filter used in the experimental setup). In order to illustrate this more clearly, we present in Fig. 8 the maximum positive frequency shift as a function of the average input power. Similar observations of a cut-off wavelength on the blue side have been made in the supercontinuum spectra of chloroform and glass [60].

For a qualitative understanding of these observations it is sufficient to analyze which parameters of the laser pulse are mainly responsible for the frequency shifts in the supercontinuum generation. Considering plane waves propagating in the nonlinear medium, the frequency deviation at a certain propagation distance z can be written as [60]:

$$\delta\omega(\tau) = -kz\frac{\partial\left(\Delta n_k + \Delta n_p\right)}{\partial\tau}, \tag{17}$$

where Δn_k and Δn_p are the contributions to the refractive index from the Kerr nonlinearity and the plasma, given by (8) and (9), respectively. For a simple estimate we can consider the Kerr nonlinear response of water as instantaneous ($g = 0$ in (8)) and take into account that the ionization of water starts from the multiphoton process of the order of $m = 5$ for the

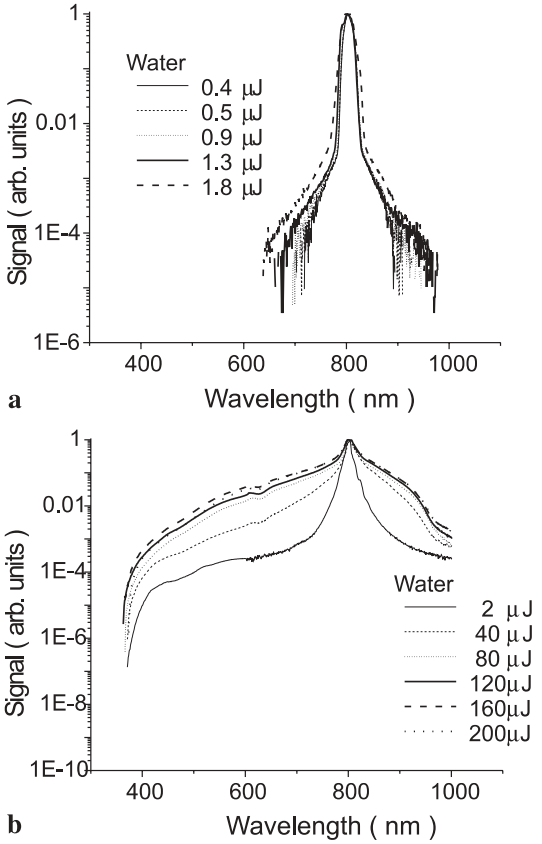

FIGURE 7 Spectra obtained for the propagation of a Ti:sapphire laser pulse with the duration 170 fs FWHM in water at various input pulse energies (see legend): **a** at low laser energies (0.4–1.8 μJ); **b** at higher laser energies (2–200 μJ)

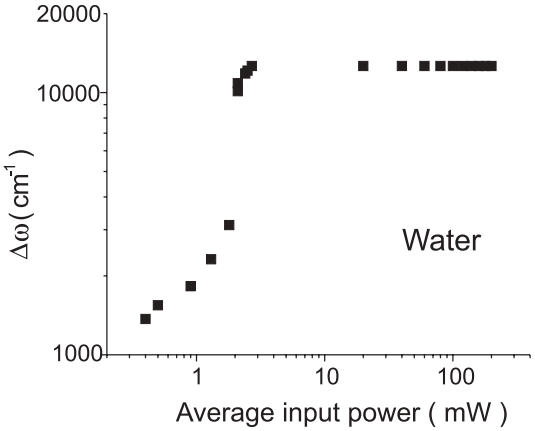

FIGURE 8 The maximum positive frequency shift $\Delta\omega_{\max}$ as a function of the average input power, obtained for the propagation of a 170-fs FWHM pulse in water. The average power of 1 mW corresponds to the energy of 1 μJ per pulse

pulse with the central wavelength of 800 nm. Then (17) can be rewritten in the form (e.g. [62]):

$$\delta\omega(\tau) = -a\frac{\partial I(\tau)}{\partial\tau} + bI^m(\tau) \ , \tag{18}$$

where $a = 4\pi n_2 kz/c$, $b = 2\pi\, e^2\beta^{(m)}N_0 kz/(m_e\omega_0^2)$ are independent of time and $\beta^{(m)}$ is the m-photon absorption coefficient of water.

At low laser energies (0.4–1.8 μJ) the symmetrical spectral broadening is due to the first term on the right-hand side of (18) (Fig. 7a). At higher laser energies the second term on the right-hand side of (18) starts to contribute to the spectral broadening and creates the asymmetric blue wing. From 2 to 200 μJ the ratio of the pulse peak power P_{peak} to the critical power for self-focusing in water $P_{\text{cr}} = 4.4$ MW [61] ranges from $P_{\text{peak}}/P_{\text{cr}} = 2.6$ to $P_{\text{peak}}/P_{\text{cr}} = 260$. The intensity growth due to self-focusing is stopped by the ionization. The threshold intensity, at which the ionization stops self-focusing, is a function of the medium and above a certain pulse energy nearly does not depend on the specifics of the pulse propagation [53]. Thus, the constant maximum positive shift, observed in Figs. 7b and 8, is the experimental evidence of the existence of such a threshold intensity or, in other words, of the peak-intensity clamping.

In (17) and (18) we have specified the main contributions to the frequency deviation $\delta\omega$ in the bulk medium. However, since this deviation is a function of the intensity gradient, all processes in the medium that affect the intensity gradients simultaneously affect the distribution of frequencies in the supercontinuum. One of such factors is material dispersion. Kolesik et al. [63] compared the extension of the supercontinuum wings generated in air in the conditions of material dispersion approximated up to the second order and the third order with the extension generated when full chromatic dispersion of air is taken into account. The error introduced by the incomplete description of the dispersion is revealed at the level of 10^{-4} of the power spectrum amplitude at the blue side. Thus, material dispersion can affect the frequency distribution in the supercontinuum generated in bulk media. Another factor that strongly influences the intensity gradient is pulse self-steepening, the effect of which on the supercontinuum was discussed in Sect. 5. However, the necessary condition for the self-steepening to be pronounced in the bulk medium is self-focusing of the radiation. Self-focusing is limited by multiphoton ionization/absorption. The resulting free-electron generation produces the blue shift described by the second terms on the right-hand sides of (17) and (18). Thus, the plasma production accompanies self-focusing in nearly all the cases of high-power ultra-short pulse propagation in bulk media. Here we note that in optical devices, such as, for example, microstructured fibers, the combination of self-steepening in the Kerr medium and material dispersion of the third and higher orders can cause an asymmetric blue shift in the power spectrum without the free-electron generation [46]. An additional factor that is sometimes considered as the possible reason for supercontinuum generation is the four-wave-mixing process [37, 38]. However, the explanation based on the four-wave-mixing process predicts that in the red side of the spectrum ($\omega < \omega_0$) longer wavelengths propagate at larger angles to the propagation axis [37]. The latter is in contradiction with the experimental observations: no conical emission was observed in the infrared [39]. In the numerical simulations, the results of which are presented below, we take into account material dispersion up to the second order and self-steepening of the pulse. Four-wave mixing is not involved in our model.

The second set of experiments in water was performed with the pulses generated by the new laser system described

in Sect. 3 (Fig. 1a). The pulses were centered at $\lambda_0 = 810$ nm with a 45-fs FWHM duration and a beam diameter of 5 mm at $1/e^2$ intensity level. The energy range was from 0.2 to 4 μJ. A series of microscope objectives was used to vary the focal length in the experiment. The resulting geometrical focusing distances were changed from 10.8 to 73.5 mm. Numerical simulations in the conditions of this experiment were performed according to the system of equations (7)–(11) and the input pulse was in the form of (14). The following parameters were used: pulse duration $2\tau_0 = 54$ fs (corresponding to 45 fs FWHM), beam radius $a_0 = 1.7$ mm, geometrical focusing distance $R_f = 16.9$ mm, 43.1 mm, and 73.5 mm, chirp parameter $\delta = 0$, the density of neutrals $N_a = 3.3 \times 10^{22}$ cm^{-3}, band-gap energy $W = 6.5$ eV, the electron collision cross section $\sigma_c = 10^{-15}$ cm^2, and the group-velocity dispersion coefficient $k''_\omega = 3 \times 10^{-28}$ s^2/cm. In the detailed experimental and numerical study [61], it is shown that there is competition between laser pulse filamentation and optical breakdown depending on the geometrical focusing condition. For a long focal length, supercontinuum generation can precede optical breakdown, while for a short focal length optical breakdown precedes supercontinuum generation. There is a critical regime for the focal length where both the phenomena can coexist together in the optical medium. In this regime, a randomly distributed white-light beam is a characteristic sign for the appearance of the filamentation and the supercontinuum generation near the breakdown plasma [51, 61].

In Fig. 9a we present the experimentally obtained (solid line) and simulated (dashed line) frequency spectra of the pulse focused in water with the geometrical focal distance of 73.5 mm. Both in the experiment and in the simulations the spectrum was integrated over the entire transverse aperture and normalized to its maximum value. The pulse energy was 3 μJ. Good qualitative agreement between the two spectra is observed. The map of spectral wavelengths corresponding to the frequency spectrum is shown in Fig. 9b. Similarly to Fig. 4, the distribution of wavelengths is presented together with the spatio-temporal intensity distribution $I(r, \tau)$ (equal-intensity contours are shown by solid lines). The upper and right insets demonstrate intensity and phase distributions in temporal and spatial cross sections, respectively. As in air, in water there is also a distinct supercontinuum source right after the self-focused front of the pulse. The location of this source is at $\tau \cong -16$ fs, $r = 0$. At the same time, in addition to this first source, there are multiple sources located in the rings produced at the trailing edge of the pulse. Several temporal phase jumps shown in the upper inset of Fig. 9b confirm the formation of the high-frequency components in the rings. The latter is manifested in the conical emission rings observed (but not studied in detail) in the present experiment in water. The radius of the ring was increasing with the decrease in the wavelength.

The increase in the amount of supercontinuum sources in water is associated with 1000 times smaller critical power for self-focusing in comparison with air. The location and the number of sources strongly depend on the geometry of the experiment. By elongating the region of filamentation in water, one can obtain smooth growth of the amount of the input pulse energy redistributed to the white light. With tight focusing a sharp increase of the white-light energy occurs at a very

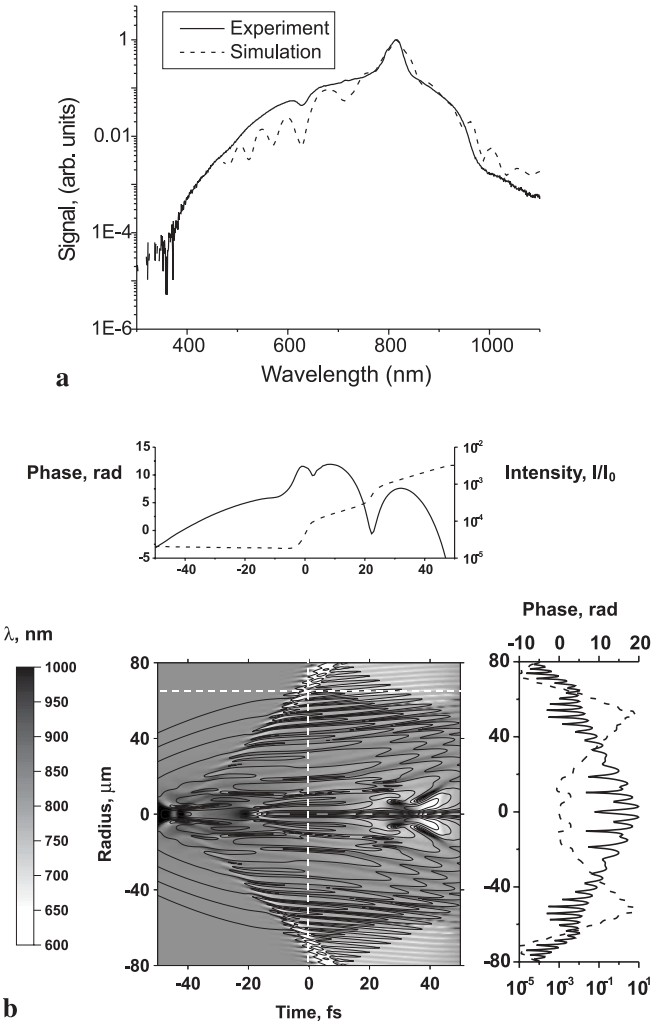

FIGURE 9 **a** Spectra obtained for the propagation of a Ti:sapphire laser pulse with the duration 45 fs FWHM and the energy of 3 μJ in water. Experiment (*solid line*), simulations (*dashed line*). In the simulations the spectrum is integrated over the whole transverse aperture and normalized to the maximum value of the spectral intensity. Propagation distance $z = -0.66$ mm from the geometrical focus position in the water cell. **b** Spatio-temporal distribution of the supercontinuum sources corresponding to the simulated spectrum shown in (a). The *solid lines* are the equal-intensity contours plotted for the following intensity values: $I_n = I_0 4^n$, where $n = -5, -4, -3, \ldots, +2$, $I_0 \approx 10^{12}$ W/cm^2. The *upper inset* corresponds to the temporal distribution of the pulse intensity (*solid line*) and phase (*dashed line*) at $r = 65$ μm; the *right inset* corresponds to the radial distribution of the intensity (*solid line*) and the phase (*dashed line*) at $\tau = 0$. Radial and temporal positions $r = 65$ μm and $\tau = 0$, respectively, are indicated by the *white dashed lines* on the map

short distance; however, the overall percentage of energy in the spectral wings might be smaller. Thus, the geometrical focusing condition of the experiment is one of the tools for governing the supercontinuum generation. Another possible tool is initial phase modulation of the laser pulse (see Sect. 8).

7 Supercontinuum from multiple filaments

In order to increase the energy of the supercontinuum in air, terawatt pulses are used in the experiments. The peak power of such pulses exceeds by several hundred times the critical power for self-focusing in air [18–20]. When such

pulses are propagated in the atmospheric conditions, a bunch of filaments is formed in the transverse beam section. Multifilamentation is a stochastic process, since the breakup of the laser pulse into the filaments is stimulated by random intensity perturbations in the transverse beam section. The source of such perturbations is imperfect initial beam quality [64] as well as the refractive-index fluctuations caused by atmospheric turbulence [65]. Filaments are formed at different distances from the output of the compressor; their positions in the transverse beam section are random. Initially, the filaments are born in the high-intensity near-axis region and afterwards at the periphery of the beam. With increasing distance from the output of the compressor, the probability to register the larger number of filaments increases [66].

Since the formation of multiple filaments results from the random intensity perturbations in the beam section, each filament can be considered as an independent source of the supercontinuum [67, 68]. The superposition of such sources gives rise to a white-light laser pulse with comparatively large power. For the propagation of a 1.6-TW, 120-fs pulse through the noble gases, the spectral power of 100–1000 MW/nm was registered in the experiment [13].

Study of the supercontinuum coherence in the course of a terawatt pulse breakup into a bunch of random filaments is important in view of femtosecond lidar applications. The measurements of the coherence of the supercontinuum produced by the laser pulse focused into different liquids have shown that the relative length of coherence of all blue spectral components is the same as the coherence length of the main laser wavelength of 800 nm [2, 68].

In the experiments on several-filament formation from laser pulses generated by a 1-TW, 10-Hz pulse of the Ti:sapphire system shown in Fig. 1a, the interference of ring structures produced by two filaments was registered [64]. The pulse duration was 45 fs and the energy 14 mJ. The regular structure of concentric rings produced by the filament developed earlier in the propagation is distorted in the vicinity of the second filament, which was formed later in the propagation (Fig. 10). The maxima of the fluence in the radial direction are due to the interference of the two divergent fields of filaments. Both fields are at the laser central frequency of 800 nm. The interference pattern is the evidence for the coherence of the two divergent fields. Therefore, the sources of the supercontinuum blue wing, which are in the rings, surrounding the filament, are also coherent.

In the experiments on the observation of the conical emission from multiple filaments we used 45-fs pulses, generated by the same laser system as in the previous experiment, but with a higher energy equal to 50 mJ. Fluence distribution in the beam at the output of the compressor was close to Gaussian with the diameter of 1.9 cm at $1/e$ fluence level. The relative value of the fluence perturbations in the beam profile did not exceed 5% and their transverse scale was of the order of 1 mm. However, due to the high peak power of the pulse ($P_{\text{peak}} = 1.1$ TW), the hot spots in the beam profile were created already after the 1-cm-thick CaF_2 the window located at the output of the vacuum pipe (see Fig. 1a). These hot spots developed into the filaments after the propagation of 4.5 m in the corridor air. With increasing propagation distance the number of filaments as well as the transverse region of their

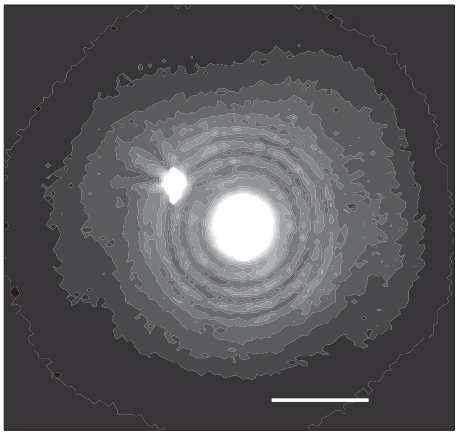

FIGURE 10 Single-shot transverse fluence distribution in a 45 fs, 14 mJ pulse at a distance $z = 87$ m from the output window to the corridor (see Fig. 1a). The number of the neutral-density filters in front of the CCD camera is chosen so as to saturate both the central and the side filaments. The interference of the transverse ring structures coming from the two filaments is observed

random formation was increasing. A detailed description of this experiment will be published elsewhere [69]. The following gives a brief account of some essential results. Figure11a shows the single-shot image taken by a Cohu 4800 CCD camera of the transverse fluence distribution at a distance $z = 30$ m from the CaF_2 window. Bright spots demonstrate the developed filaments, while pale spots show the filaments, which are still under development.

To register the supercontinuum conical emission we use a Canon A 40 digital camera. The digital camera image obtained at the same distance $z = 30$ m as the CCD image is shown in Fig. 11b. Colored conical emission rings are encompassing the bunch of filaments. The radius of the ring increases with increasing spectral frequency as in the case of a single filament. However, unlike the case of the single-filament regime, there are interference maxima in the radial direction. Note that the interference pattern in Fig. 11b is registered for the spectral components of the supercontinuum and not for the laser frequency as in Fig. 10. The interference picture for the bunch of filaments has a more complex structure than in the case of the two-filament regime. The most contrast maxima are formed near the most remote filament as the result of the interference between the supercontinuum formed by this particular filament and the rest of the filaments in the bunch. With increasing propagation distance and, hence, the number of filaments, the interference maxima become less contrasty. The interference pattern was changing from pulse to pulse due to the random process of the filament formation in the beam section.

On the basis of these results the following scenario of supercontinuum generation from multiple filaments can be deduced. In each pulse the supercontinuum sources are created, which are located randomly in the transverse beam section. The phase shift between the same spectral components generated by different sources depends on the source position in both longitudinal and transverse directions. Since the filament formation position depends on the beam quality and refractive-index fluctuations in the atmosphere, the phase shift

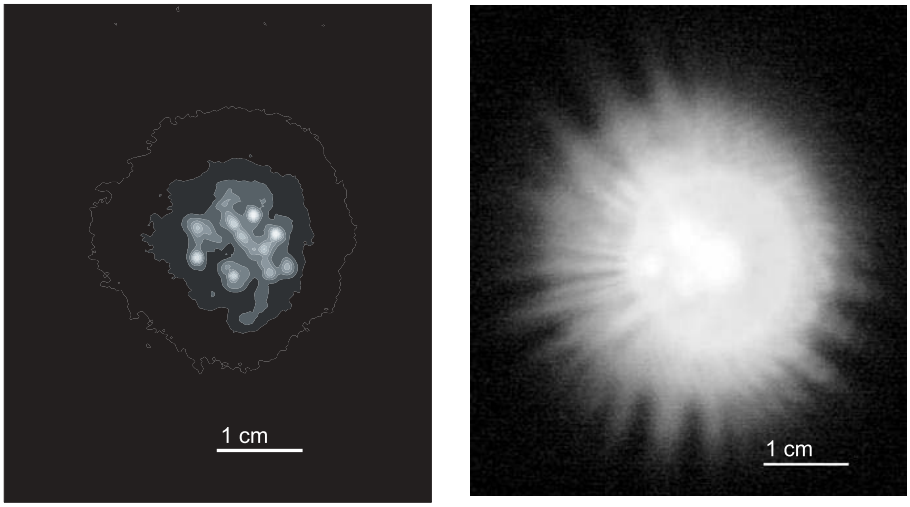

FIGURE 11 **a** Single-shot transverse fluence distribution in a 45-fs, 50-mJ pulse at a distance $z = 30$ m from the output window to the corridor. The number of the neutral-density filters in front of the CCD camera is chosen so as none of the multiple filaments is saturated. **b** The digital camera image of the transverse fluence distribution for the same laser pulse parameters and propagation distance as in **a**

is a random value from shot to shot. However, during a single laser pulse, the supercontinuum sources remain coherent since they originate from the same coherent pulsed radiation. Refractive-index fluctuations in the atmosphere can be considered as frozen on the femtosecond time scale. As the result, in the course of multifilamentation of each pulse we observe the interference pattern from several supercontinuum sources. With propagation distance the interference pattern can experience transformations due to the change in the phase shift between these sources. Besides, from pulse to pulse the phase shift changes randomly due to the variations in the field of atmospheric refractive-index fluctuations and the intensity perturbations at the laser system output. Therefore, the interference pattern might be different in each single pulse. For a train of pulses, the interference picture and, hence, the directional diagram of the supercontinuum, is averaged and has an axially symmetric distribution in the form of a narrow cone. The averaged power of spectral components is proportional to the number of filaments in the beam.

8 Control of the supercontinuum generation by means of initial pulse chirp

From the point of view of applications, it is important to control the nonlinear-optical transformation of a femtosecond laser pulse into the supercontinuum. In the experiment [19], performed in the actual atmospheric conditions, the supercontinuum generation was controlled simply by geometric focusing of the beam. Initial wavefront curvature to a large extent defines the filament starting position and regularizes the formation of a bunch of filaments in the conditions of turbulence.

Initially, the effect of the pulse phase modulation in the time domain (i.e. temporal up and down chirps of the pulse) on the distance between the laser system output and the filament starting position was experimentally registered in [70]. The results showed that, at a constant pulse energy, when the chirp was swept from a negative value to a positive value, the distance passed through a minimum at the position of zero chirp (Fig. 12). This was explained in the following way. With either negative or positive chirp, the pulse has a lower peak power. Hence it takes a longer propagation distance to reach the self-focus or the starting point of the filament. In the case of negative chirp, the compensation of the chirp by linear dispersion during propagation in the neutral air also played a role. In the outdoor experiments [71] the filament distance was increased from 10 to 40 m by means of the initial pulse chirp. Measurements of the supercontinuum [18] showed that the usage of the negatively chirped pulses leads to the increase in the conversion efficiency to the near-infrared part of the spectrum.

We have performed a numerical study of the filamentation and supercontinuum generation control by means of the initial pulse chirp. The parameters of the radiation were $\lambda = 800$ nm, pulse energy $= 60$ mJ, duration of a transform-limited pulse at $1/e$ level of intensity was $\tau_0 = 42$ fs, beam radius was $a_0 = 1.5$ cm. The chirped pulse duration $\tau_p(\delta)$ was defined from the condition of a constant spectral width $\Delta\omega$ [56]. If the parameter $\delta > 0$, the phase modulation is positive and in the medium with normal dispersion, as air, and the linear propagation regime, the duration of the chirped pulse increases. If the parameter $\delta < 0$, the phase modulation is negative, and in air the pulse duration decreases and then increases. Without

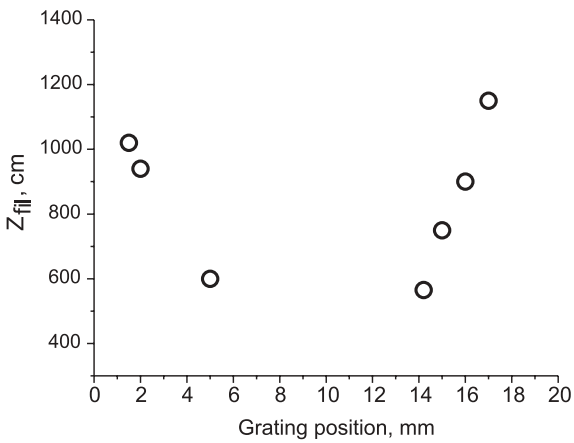

FIGURE 12 Dependence of the beginning of the filament on the spacing between the parallel grating pair in the compressor. z_{fil} is the distance from the output of the compressor to the beginning of the filament. Input beam radius at $1/e$ intensity level $a_0 = 2.1$ mm; pulse energy: 6.2 mJ; optimum pulse duration: 250 fs. Positive chirp is at larger grating positions (towards the right-hand side of the minimum); negative chirp towards opposite positions

the nonlinear effects, the pulse duration is a minimum at a distance equal to the compression length $L_{\mathrm{comp}}(\delta)$ [41].

The conversion efficiency of the radiation at the laser frequency to the supercontinuum is defined by the whole process of filamentation and depends on the filament length as well as the presence of the regions with high temporal gradients of the electric field. The effect of the initial pulse chirp on the filamentation is revealed simultaneously through the two factors: static and dynamic.

The static factor is in the redistribution of the power in the pulse at the output of the compressor. Indeed, for the chirped pulse, $\tau_{\mathrm{p}}(\delta) > \tau_{\mathrm{p}}(0)$ and the peak power $P_{\mathrm{peak}}(\delta)$ decreases with increasing absolute value of δ according to the relation:

$$P_{\mathrm{peak}}(\delta) = \pi a_0^2 I_0 \tau_0 / \tau_{\mathrm{p}}(\delta) \; . \tag{19}$$

As the peak power decreases, the self-focusing length $L_{\mathrm{sf}}(\delta)$ [41] and, hence, the filament formation and supercontinuum generation distance increase.

The dynamic manifestation of the initial pulse chirp is in the change of the light-field localization in time in the dispersive medium. The character of these changes depends on the chirp sign. Figure13 shows the fluence, peak intensity, and supercontinuum energy distributions along the propagation axis z for different values of the chirped pulse duration $\tau_{\mathrm{p}}(\delta)$. In each panel the first plot corresponds to the fluence distribution, while the second plot shows the change of the pulse peak intensity (thin solid line plotted against the left vertical axis) and the supercontinuum energy (thick solid line plotted against the right vertical axis). Note that the fluence is the value that is usually measured in the experiments. One can see that, independently of the initial pulse chirp, the fluence distribution along the filament is nonmonotonic and represents the sequence of bright spots. In the case of the positive initial phase modulation ($\delta > 0$) the spreading out of the pulse in air is stronger than in the case of the transform-limited pulse (compare Fig. 13a and b). Simultaneously, such localization leads to the elongation of the filament in comparison with the transform-limited pulse.

In the case of the negative initial phase modulation ($\delta < 0$), the compression of the pulse takes place and its effect on the filamentation depends on the relation between the compression length $L_{\mathrm{comp}}(\delta)$ and the self-focusing length $L_{\mathrm{sf}}(\delta)$. If $L_{\mathrm{comp}}(\delta) \ll L_{\mathrm{sf}}(\delta)$ then the pulse contraction due to the material dispersion precedes self-focusing and the filamentation develops similarly to the case of the transform–limited pulse. If $L_{\mathrm{comp}}(\delta) \gg L_{\mathrm{sf}}(\delta)$ then the effect of the dispersion-provided contraction on the filamentation is negligible.

The optimum situation for the control of the filamentation is the comparable values of compression and self-focusing lengths with $L_{\mathrm{comp}}(\delta) \geq L_{\mathrm{sf}}(\delta)$. In this case in the preliminary stretched pulse ($\tau_{\mathrm{p}}(\delta) > 200$ fs for our parameters), the energy is gradually localized in time in the course of the filamentation. As the result, we obtain the increase of the filament-formation distance and the simultaneous increase in the length of the filament in comparison with the transform–limited pulse (Fig. 13b and c). Indeed, in the course of the pulse temporal compression, the power in the front slices becomes higher with propagation distance. A number of slices, which at the laser system output did not have enough power for self-focusing, accumulate the power $P > P_{\mathrm{cr}}$ at some propagation distance. Therefore, self-focusing of these slices is delayed in distance, and the result of this is the lengthening of the filament.

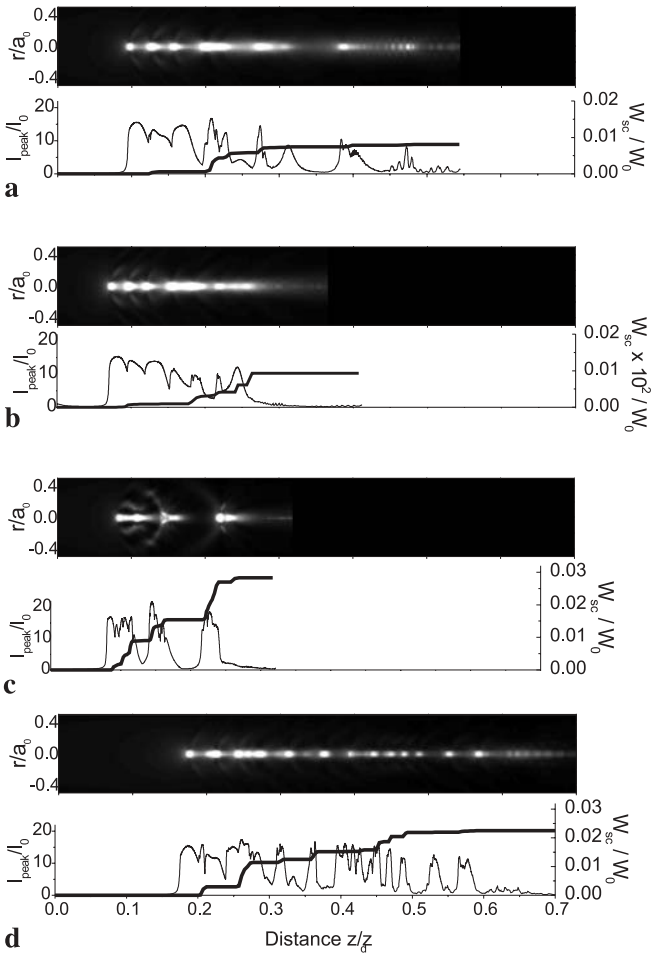

FIGURE 13 In **a** to **d** the *upper plot* shows the gray-scale map of the fluence distribution in the filament along the propagation axis z. The *lower plot* shows the dependence of the pulse peak on-axis intensity I_{peak} (*thin solid line* plotted against the *left vertical axis*) and the supercontinuum energy W_{sc} (*thick solid line* plotted against the *right vertical axis*) on distance z. Pulse energy 60 mJ, $I_0 \approx 10^{13}$ W/cm^2, transform limited pulse duration $\tau_0 = 21$ fs. At $z = 0$ the pulse has initial phase modulation **a** $\delta > 0$, $\tau_{\mathrm{p}}(\delta) = 100$ fs; **b** $\delta = 0$, $\tau_{\mathrm{p}}(\delta) = 21$ fs; **c** $\delta < 0$ (negative chirp), $\tau_{\mathrm{p}}(\delta) = 150$ fs; **d** $\delta < 0$ (negative chirp), $\tau_{\mathrm{p}}(\delta) = 600$ fs

In the simulations for the negatively chirped pulse with $\tau_{\mathrm{p}}(\delta) \approx 150$ fs, the compression length $L_{\mathrm{comp}}(\delta)$ nearly coincides with the self-focusing length $L_{\mathrm{comp}}(\delta)$. The localization of energy in both space and time occurs simultaneously. In the case of such spatio-temporal 'focusing' the filament is degenerated into several bright maxima and its length is decreased even in comparison with the case of the transform-limited pulse (compare Fig. 13b and c).

Temporal compression of the pulse essentially affects the spatio-temporal gradients of the intensity as well as the phase and, hence, the conversion efficiency of the initial laser pulse to the supercontinuum. This is confirmed by the simulation results for the peak intensity

$$I_{\mathrm{peak}}(r = 0, z) = \max_{\tau} \{ I(r = 0, z, \tau) \} \; , \tag{20}$$

and the energy contained on the blue side of the supercontinuum

$$W_{sc}(z) = \int_{\lambda_{min}}^{\lambda_{max}} S(\lambda, z)\, d\lambda\,, \qquad (21)$$

where $\lambda_{min} = 500$ nm and $\lambda_{max} = 700$ nm. As mentioned earlier, the values (20) and (21) are shown in the second plots of panels (a)–(d) in Fig. 13.

By following the dependence of the supercontinuum energy on distance, one can notice that for all four values of the chirped pulse duration $\tau_p(\delta)$ the growth of the supercontinuum energy W_{sc} occurs at the same values of z as the jumps in the peak on-axis intensity I_{peak}.

In the transform-limited pulse the change of the peak intensity along the filament is comparatively smooth. The leading fronts of the intensity are not very steep and the corresponding phase gradients are moderate. The resulting conversion efficiency to the supercontinuum is low and the energy contained on the blue side of the supercontinuum W_{sc} does not exceed 0.01% of the initial pulse energy W_0 (Fig. 13b).

In the case of the positive phase modulation the intensity peaks at the end of the filament lead to the increase of the supercontinuum energy up to 1% of the initial pulse energy W_0 (Fig. 13a).

In the case of the negative phase modulation the filament consists of a number of contrast intensity maxima. The corresponding temporal gradients of the intensity and the phase are large enough to lead to the increase in the supercontinuum energy up to 3% of W_0 (Fig. 13c and d). The highest supercontinuum energy is achieved in the shortest filament with the chirped pulse duration $\tau_p(\delta) = 150$ fs (Fig. 13c). This filament consists of the three separated regions with high peak intensity. In these regions high localization of the radiation provided due to both temporal compression and self-focusing is replaced by the plasma-induced defocusing. The resulting phase gradients lead to the effective conversion of the laser pulse energy into the supercontinuum energy.

Thus, in the case of the filamentation of the negatively chirped pulses, the efficiency in the generation of the high-frequency components of the supercontinuum is much higher than in the case of the transform-limited pulse. The supercontinuum energy increases by two orders of magnitude in a wide range of the negatively chirped pulse duration $\tau_p(\delta)$ from $\tau_p(\delta) = 100$ fs to $\tau_p(\delta) = 800$ fs.

Note that the energy contained on the red side of the supercontinuum is weakly dependent on the initial phase modulation of the laser pulse. This is due to the fact that the long-wavelength components of the supercontinuum are generated early in the front of the pulse. The steepness of this particular region is nearly not changing in the case of the filamentation of initially chirped pulses.

9 Conclusions

We have performed an experimental and numerical study of the nonlinear-optical transformation of a femtosecond laser pulse in condensed and gaseous media by the example of water and atmospheric air, respectively. We have shown that the spatio-temporal modification of the pulse shape and the corresponding frequency angular modification of the pulse spectrum result from the same nonlinear-interaction of the laser radiation with the medium. This interaction is due to the joint effect of the Kerr nonlinearity of neutrals and the nonlinearity of the laser-produced plasma as well as such propagation effects as dispersion, diffraction, and self-steepening of the pulse fronts. Formation of filaments with high spatio-temporal localization of energy provides us with the large nonlinear interaction length, which leads to a dramatic change of the pulse shape and transformation of the pulse spectrum to the supercontinuum.

Transformation of a narrow laser pulse spectrum into the continuum is due to the self-phase modulation of the light field in both space and time. The temporal phase gradient is responsible for the new frequency components, while the spatial gradient is responsible for the angular divergence of these newborn frequencies. As a result, the supercontinuum cone emission is observed. High spatio-temporal localization of the radiation, which is observed in the experiments, results from the dynamic process of the replenishment of energy in the filament. The replenishment process encompasses a significant transverse area, which is larger than the beam diameter at the laser system output. In this region the dynamic ring structure is formed in the intensity distribution. The correct numerical consideration of the low-intensity background at the beam periphery allowed us to obtain satisfactory quantitative agreement between the simulated and experimentally registered supercontinuum conical emission angles. Both the experiment and the simulations were performed for the propagation of a 250-fs, 10-mJ pulse with a central wavelength of 800 nm and a beam radius of 3.5 mm at $1/e$ intensity level.

We have shown that the sources of the supercontinuum blue wing are in the ring structure surrounding the filament. Another contribution to the high-frequency spectral components comes from the trailing edge of the pulse, where the positive frequency shift originates due to the shock formation at the back of the pulse. This source of the supercontinuum does not reveal the increase of the divergence angle with increasing spectral frequency. The newborn high frequencies mainly propagate along the beam axis.

In water we experimentally obtained two characteristic features of the spectral broadening. At low laser energies (0.4–1.8 μJ) the spectra of a 170-fs pulse show a symmetrical broadening towards lower and higher frequencies, while at higher pulse energies (2–200 μJ) the typical long pedestal emerges on the blue side. The minimum wavelength of the blue spectral wing (≈ 400 nm) remains almost constant for an increase in the pulse energy by two orders of magnitude. This is the evidence for the peak intensity clamping inside the filaments produced by an ultra-short pulse in water. Numerical simulations of a 45-fs, 3-μJ pulse propagation in water showed good qualitative agreement between the simulated and experimentally obtained frequency spectra. Multiple sources of the high-frequency components of the supercontinuum are found to be located in the rings formed due to the defocusing of the pulse in the plasma, produced due to both multiphoton ionization and the avalanche.

In the experiments on multiple filamentation of a 45-fs pulse with the energy of 14–50 mJ and the central wavelength

of 810 nm we have registered the phenomenon of the interference of the conical emission spectral components, generated by different filaments from the same bunch of filaments. Therefore, the white-light laser pulses produced by multiple filaments are coherent in spite of the random character of multifilamentation associated with the beam quality and refractive-index fluctuations in the turbulent atmosphere.

The conversion efficiency of the radiation to the supercontinuum is defined by the whole process of filamentation and depends on the filament length as well as the presence of the regions with high temporal gradients of the light field. If the initial pulse is negatively chirped, the efficiency in the generation of the high-frequency components of the supercontinuum is much higher than in the case of the transform-limited pulse. Numerical simulations of the propagation of a 42-fs, 60-mJ pulse in air showed that the supercontinuum energy can be increased by more than an order of magnitude in the case of the negatively chirped pulses.

ACKNOWLEDGEMENTS VPK, OGK, and ISG acknowledge the support of the Russian Foundation for Basic Research, Grant No. 00-02-17497; VPK, OGK, and SLC acknowledge the support of the NATO Linkage Grant No. PST.CLG.976981; SLC and WL are also supported in Canada by NSERC, DRDC-Valcartier, CIPI, Canada Research Chair, and FCAR. NA was supported by ARO under Contract No. DAAD 19–02 C-0091. The support of the Alexander von Humboldt Foundation via a Research Award to SLC and a Feodor Lynen fellowship to AB is highly appreciated.

REFERENCES

1 R.R. Alfano (Ed.): *The Supercontinuum Laser Source* (Springer, Berlin 1989)
2 S.L. Chin, A. Brodeur, S. Petit, O.G. Kosareva, V.P. Kandidov: J. Nonlinear Opt. Phys. Mater. **8**, 121 (1999)
3 R.R. Alfano, S.L. Shapiro: Phys. Rev. Lett. **24**, 592 (1970)
4 P.B. Corkum, C. Rolland, T. Srinavasan-Rao: Phys. Rev. Lett. **57**, 2268 (1986)
5 A.A. Babin, D.V. Kartashov, A.M. Kiselev, V.V. Lozhkarev, A.N. Stepanov, A.M. Sergeev: Appl. Phys. B **75**, 509 (2002)
6 J.K. Ranka, R.S. Windeler, A.J. Stentz: Opt. Lett. **25**, 25 (2000)
7 A.B. Fedotov, A.M. Zheltikov, A.P. Tarasevitch, D. von der Linde: Appl. Phys. B **73**, 181 (2001)
8 D.A. Akimov, A.A. Ivanov, M.V. Alfimov, S.N. Bagayev, T.A. Birks, W.J. Wadsworth, P.St.J. Russell, A.B. Fedotov, V.S. Pivtsov, A.A. Podshivalov, A.M. Zheltikov: JETP Lett. **74**, 460 (2001)
9 A. Braun, G. Korn, X. Liu, D. Du, J. Squier, G. Mourou: Opt. Lett. **20**, 73 (1995)
10 E.T.J. Nibbering, P.F. Curley, G. Grillon, B.S. Prade, M.A. Franco, F. Salin, A. Mysyrowicz: Opt. Lett. **21**, 62 (1996)
11 A. Brodeur, C.Y. Chien, F.A. Ilkov, S.L. Chin, O.G. Kosareva, V.P. Kandidov: Opt. Lett. **22**, 304 (1997)
12 B. La Fontaine, F. Vidal, Z. Jiang, C.Y. Chien, D. Corntois, A. Desparois, T.W. Johnston, J.-C. Kieffer, H. Pepin, H.P. Mercure: Phys. Plasmas **6,** 1815 (1999)
13 H. Nishioka, W. Odajima, Ken-ichi Ueda, H. Takuma: Opt. Lett. **20**, 2505 (1995)
14 S. Tzortzakis, B. Lamouroux, A. Chiron, M. Franco, B. Prade, A. Mysyrowicz, S.D. Moustaizis: Opt. Lett. **25**, 1270 (2000)
15 O.G. Kosareva, V.P. Kandidov, A. Brodeur, S.L. Chin: J. Nonlinear Opt. Phys. Mater. **6**, 485 (1997)
16 M. Mlejnek, E.M. Wright, J.V. Moloney: Opt. Lett. **23**, 382 (1998)
17 A. Chiron, B. Lamoroux, R. Lange, J.-F. Ripoche, M. Franco, B. Prade, G. Bonnaud, G. Riazuelo, A. Mysyrowicz: Eur. Phys. J. D **6**, 383 (1999)
18 J. Kasparian, R. Sauerbrey, D. Mondelain, S. Niedermeier, J. Yu, J.-P. Wolf, Y.-B. André, M. Franco, B. Prade, S. Tzortzakis, A. Mysyrowicz, M. Rodriguez, H. Wille, L. Wöste: Opt. Lett. **25**, 1397 (2000)
19 L. Wöste, C. Wedekind, H. Wille, P. Rairoux, B. Stein, S. Nikolov, C. Werner, S. Niedermeier, F. Ronneberger, H. Schillinger, R. Sauerbrey: Laser Optoelectron. **5,** 29 (1997)
20 P. Rairoux, H. Schillinger, S. Niedermeier, M. Rodriguez, F. Ronneberger, R. Sauerbrey, B. Stein, D. Waite, C. Wedekind, H. Wille, L. Wöste, C. Ziener: Appl. Phys. B **71**, 573 (2000)
21 G. Yang, Y.R. Shen: Opt. Lett. **9**, 510 (1984)
22 P.B. Corkum, C. Rolland: IEEE J. Quantum Electron. **QE-25**, 2634 (1989)
23 J.J. Glownia, J. Misewich, P.P. Sorokin: J. Opt. Soc. Am. B **3**, 1573 (1986)
24 F.A. Ilkov, L.Sh. Ilkova, S.L. Chin: Opt. Lett. **18**, 681 (1993)
25 W. Liu, Q. Luo, S.L. Chin: Chin. Opt. Lett. **1**, 56 (2003)
26 T. Nguyen, A. Saliminia, W. Liu, S.L. Chin, R. Vallee: Opt. Lett. (2003) accepted for publication
27 N. Bloembergen: Opt. Commun. **8**, 285 (1973)
28 W.M. Wood, C.W. Siders, M.C. Downer: IEEE Trans. Plasma Sci. **21**, 20 (1993)
29 S.P. Le Blanc, R. Sauerbrey, S.C. Rae, K. Burnett: J. Opt. Soc. Am. B **10**, 801 (1993)
30 V.P. Kandidov, O.G. Kosareva, S.A. Shlyonov: J. Nonlinear Opt. Phys. Mater. **12**, 119 (1994)
31 S.C. Rae: Opt. Commun. **104**, 330 (1994)
32 P.B. Corkum, C. Rolland: In *Atomic and Molecular Processes with Short Intense Laser Pulses*, ed. by A.D. Bandrauk (NATO ASI Ser. Phys. B **171**) (Plenum, New York 1987) p. 157
33 O.G. Kosareva, V.P. Kandidov, S.A. Shlenov: In *Superintense Laser–Atom Physics IV*, ed. by H.G. Muller, M.V. Fedorov (NATO ASI Ser.) (Kluwer, Dordrecht 1996) pp. 489–502
34 C.W. Siders, N.C. Turner III, M.C. Downer, A. Babin, A. Stepanov: J. Opt. Soc. Am. B **13**, 330 (1996)
35 A.B. Fedotov, N.I. Koroteev, M.M.T. Loy, X. Xiao, A.M. Zheltikov: Opt. Commun. **133**, 587 (1997)
36 I. Golub: Opt. Lett. **15**, 305 (1990)
37 Q. Xing, K.M. Yoo, R.R. Alfano: Appl. Opt. **32**, 2087 (1993)
38 G.G. Luther, A.C. Newell, J.V. Moloney, E.M. Wright: Opt. Lett. **19**, 789 (1994)
39 O.G. Kosareva, V.P. Kandidov, A. Brodeur, C.Y. Chien, S.L. Chin: Opt. Lett. **22**, 1332 (1997); I.S. Golubtsov, V.P. Kandidov, O.G. Kosareva: Atmos. Ocean. Opt. **14**, 966 (2001)
40 E.T.J. Nibbering, G. Grillon, M.A. Franco, B.S. Prade, A. Mysyrowicz: J. Opt. Soc. Am. B **14**, 650 (1997)
41 S.A. Akmanov, V.A. Vyslouh, A.S. Chirkin: *Optics of Femtosecond Laser Pulses* (American Institute of Physics, New York 1992)
42 T. Brabec, F. Krausz: Phys. Rev. Lett. **78**, 3282 (1997)
43 A.L. Gaeta: Phys. Rev. Lett. **84**, 3582 (2000)
44 N. Akozbek, M. Scalora, C.M. Bowden, S.L. Chin: Opt. Commun. **191**, 353 (2001)
45 I.S. Golubtsov, O.G. Kosareva: J. Opt. Technol. **69**, 462 (2002)
46 A.L. Gaeta: Opt. Lett. **27**, 924 (2002)
47 Y.R. Shen: *The Principles of Nonlinear Optics* (Wiley, New York 1984)
48 P.A. Oleinikov, V.T. Platonenko: Laser Phys. **3**, 618 (1993)
49 H. Schillinger, R. Sauerbrey: Appl. Phys. B **68**, 753 (1999)
50 S. Tzortzakis, M.A. Franco, Y.-B. André, A. Chiron, B. Lamouroux, B.S. Prade, A. Mysyrowicz: Phys. Rev. E **60**, R3505 (1999)
51 W. Liu, O. Kosareva, I.S. Golubtsov, A. Iwasaki, A. Becker, V.P. Kandidov, S.L. Chin: Appl. Phys. B **75**, 595 (2002)
52 V.P. Kandidov, O.G. Kosareva, S.A. Shlyonov: Quantum Electron. **24**, 905 (1994)
53 J. Kasparian, R. Sauerbrey, S.L. Chin: Appl. Phys. B **71**, 877 (2000)
54 A.M. Perelomov, V.S. Popov, M.V. Terent'ev: Sov. Phys. JETP **23**, 924 (1966)
55 A. Talebpour, J. Yang, S.L. Chin: Opt. Commun. **163**, 29 (1999)
56 I.S. Golubtsov, V.P. Kandidov, O.G. Kosareva: Quantum Electron. **33**, N6, 550 (2002)
57 A. Becker, N. Aközbek, K. Vijayalakshmi, E. Oral, C.M. Bowden, S.L. Chin: Appl. Phys. B **73**, 287 (2001)
58 H.R. Lange, A. Chiron, J.-F. Ripoche, A. Mysyrowicz, P. Breger, P. Agostini: Phys. Rev. Lett. **81**, 1611 (1998)
59 V.P. Kandidov, O.G. Kosareva, A.A. Koltun: Quantum Electron. **33**, 69 (2003)
60 W. Liu, S. Petit, A. Becker, N. Aközbek, C.M. Bowden, S.L. Chin: Opt. Commun. **202**, 189 (2002)
61 W. Liu, O. Kosareva, I.S. Golubtsov, A. Iwasaki, A. Becker, V.P. Kandidov, S.L. Chin: Appl. Phys. B **76**, 215 (2003)

62 C. Rulliere (Ed.): *Femtosecond Laser Pulses* (Springer, Berlin 1998) p. 47
63 M. Kolesik, J.V. Moloney, M. Mlejnek: Phys. Rev. Lett. **89**, 283902 (2002)
64 S.L. Chin, S. Petit, W. Liu, A. Iwasaki, M.-C. Nadeau, V.P. Kandidov, O.G. Kosareva, K.Yu. Andrianov: Opt. Commun. **210**, 329 (2002)
65 S.L. Chin, A. Talebpour, J. Yang, S. Petit, V.P. Kandidov, O.G. Kosareva, M.P. Tamarov: Appl. Phys. B **74**, 67 (2002)
66 S.A. Shlenov, V.P. Kandidov, O.G. Kosareva: 'Multifilamentation of High-Power Femtosecond Laser Pulses In the Turbulent Atmosphere'. In: Tech. Dig. Int. Quantum Electronics Conf. IQEC/LAT-2002, Moscow, Russia, 22–27 June 2002, p. 53
67 A. Brodeur, F.A. Ilkov, S.L. Chin: Opt. Commun. **129**, 193 (1996)
68 S.L. Chin, S. Petit, F. Borne, K. Miyazaki: Jpn. J. Appl. Phys. **38**, L126 (1999)
69 W. Liu, S. Hosseini, Q. Luo, B. Ferland, S.L. Chin: submitted to Appl. Phys. B
70 S.L. Chin: 'A study of the fundamental science underlying the transport of intense femtosecond laser pulses in the atmosphere'. Final Report for Grant No. DAAG55-97-1-0404, 1 October 1997 to 31 December 1998, submitted to the Army Research Office, Research Triangle Park, NC, USA, 20 January 1999
71 H. Wille, M. Rodriguez, J. Kasparian, D. Mondelain, J. Yu, A. Mysyrowicz, R. Sauerbrey, J.P. Wolf, L. Wöste: Eur. Phys. J. – Appl. Phys. **20**, 183 (2002)